



**HAL**  
open science

## Kepler K2 Campaign 9 - I. Candidate short-duration events from the first space-based survey for planetary microlensing

I. Mcdonald, E. Kerins, R. Poleski, M. T. Penny, D. Specht, S. Mao, P. Fouqué, W. Zhu, W. Zang

### ► To cite this version:

I. Mcdonald, E. Kerins, R. Poleski, M. T. Penny, D. Specht, et al.. Kepler K2 Campaign 9 - I. Candidate short-duration events from the first space-based survey for planetary microlensing. Monthly Notices of the Royal Astronomical Society, 2021, 505, pp.5584-5602. 10.1093/mnras/stab1377 . insu-03672405

**HAL Id: insu-03672405**

**<https://insu.hal.science/insu-03672405>**

Submitted on 19 May 2022

**HAL** is a multi-disciplinary open access archive for the deposit and dissemination of scientific research documents, whether they are published or not. The documents may come from teaching and research institutions in France or abroad, or from public or private research centers.

L'archive ouverte pluridisciplinaire **HAL**, est destinée au dépôt et à la diffusion de documents scientifiques de niveau recherche, publiés ou non, émanant des établissements d'enseignement et de recherche français ou étrangers, des laboratoires publics ou privés.

# Kepler K2 Campaign 9 – I. Candidate short-duration events from the first space-based survey for planetary microlensing

I. McDonald<sup>1</sup>,<sup>2</sup>\*, E. Kerins,<sup>1</sup> R. Poleski,<sup>3</sup> M. T. Penny<sup>4</sup>, D. Specht<sup>1</sup>, S. Mao,<sup>5,6</sup> P. Fouqué,<sup>7,8</sup> W. Zhu<sup>5,9</sup> and W. Zang<sup>5</sup>

<sup>1</sup>Jodrell Bank Centre for Astrophysics, Alan Turing Building, University of Manchester, Manchester M13 9PL, UK

<sup>2</sup>Open University, Walton Hall, Kents Hill, Milton Keynes MK7 6AA, UK

<sup>3</sup>Astronomical Observatory, University of Warsaw, Al. Ujazdowskie 4, P-00-478 Warszawa, Poland

<sup>4</sup>Louisiana State University, 261-B Nicholson Hall, Tower Dr., Baton Rouge, LA 70803-4001, USA

<sup>5</sup>Department of Astronomy, Tsinghua University, Beijing 100084, China

<sup>6</sup>National Astronomical Observatories, Chinese Academy of Sciences, Beijing 100101, China

<sup>7</sup>Université de Toulouse, UPS-OMP, IRAP, F-31555 Toulouse, France

<sup>8</sup>CFHT Corporation, 65-1238 Mamalahoa Hwy, Kamuela, HI 96743, USA

<sup>9</sup>Canadian Institute for Theoretical Astrophysics, University of Toronto, 60 St George Street, Toronto, ON M5S 3H8, Canada

Accepted 2021 May 11. Received 2021 May 10; in original form 2020 December 22

## ABSTRACT

We present the first short-duration candidate microlensing events from the *Kepler K2* mission. From late April to early July 2016, Campaign 9 of *K2* obtained high temporal cadence observations over a  $3.7 \text{ deg}^2$  region of the Galactic bulge. Its primary objectives were to look for evidence of a free-floating planet (FFP) population using microlensing, and demonstrate the feasibility of space-based planetary microlensing surveys. Though *Kepler K2* is far from optimal for microlensing, the recently developed MCPM photometric pipeline enables us to identify and model microlensing events. We describe our blind event-selection pipeline in detail and use it to recover 22 short-duration events with effective time-scales  $t_{\text{eff}} < 10 \text{ d}$  previously announced by the OGLE and KMTNet ground-based surveys. We also announce five new candidate events. One of these is a caustic-crossing binary event, modelled in a companion study. The other four have very short durations ( $t_{\text{eff}} < 0.1 \text{ d}$ ) typical of an Earth-mass FFP population. Whilst *Kepler* was not designed for crowded-field photometry, the *K2C9* data set clearly demonstrates the feasibility of conducting blind space-based microlensing surveys towards the Galactic bulge.

**Key words:** gravitational lensing: micro – planets and satellites: detection – brown dwarfs – planetary systems – stars: statistics – Galaxy: bulge.

## 1 INTRODUCTION

Free-floating planetary-mass objects (FFPs) may represent the end-states of disrupted exoplanetary systems (e.g. Rasio & Ford 1996) and ‘failed’ stars (Whitworth & Zinnecker 2004; Gahm et al. 2007). Except for the very young and most massive planets (e.g. Lucas & Roche 2000; Bihain et al. 2009; Quanz et al. 2010; Peña Ramírez, Béjar & Zapatero Osorio 2016; Schneider et al. 2016), such objects are too faint to be detected directly, and their identification relies on gravitational microlensing (e.g. Han et al. 2004; Mróz et al. 2017), whereby the planet traverses the observer’s line of sight towards a background star. The background star is brightened by a Paczyński (1986) curve, with a characteristic time-scale ( $t_E = R_E/v_{\text{rel}}$ ), defined by an Einstein (1936) radius ( $R_E$ ) and a relative source–lens tangential velocity ( $v_{\text{rel}}$ ).  $R_E$  depends on the lens mass, and the relative separations of observer, lens, and source (Section 3.2). As  $v_{\text{rel}}$  and lens distance are generally unknown, FFP candidates are observationally defined by events with short  $t_E$ , unless second-order effects can be

quantified, frequently from simultaneous ground- and space-based measurements (e.g. detection of parallax effects, relative velocities inferred from finite-source effects, etc.; Han 2006; Di Stefano 2012; Udalski et al. 2015b; Henderson & Shvartzvald 2016). Contaminants, including high-velocity stars and planets in wide orbits, can enter the data set (Di Stefano 2012; Clanton & Gaudi 2017). Thus, FFP abundances are normally calculated on a statistical basis, as an excess number of events with short  $t_E$ .

Ejected high-mass (gas-giant) planets can only account for a relatively small number of FFPs (Veras & Raymond 2012; Ma et al. 2016), hence an abundance of low-mass lenses would indicate the stellar initial-mass function turns up at masses below the brown dwarf ‘desert’ (e.g. Halbwachs et al. 2000). FFP abundances have been variously estimated as twice (Sumi et al. 2011) or less than a quarter (Mróz et al. 2017) as common as main-sequence stars. One source of tension between the two results arises from differing treatments of faint, highly blended events, where the lensed star contributes less than 10 per cent of the incident flux on that part of the imaging detector: Mróz et al. (2017) claim that the  $t_E$  of such events cannot be reproduced satisfactorily, leading to an artificial excess of short-time-scale events. Such events may be characterized by the alternative

\* E-mail: [iain.mcdonald-2@manchester.ac.uk](mailto:iain.mcdonald-2@manchester.ac.uk)

measure  $t_{\text{eff}} = t_E u_0$  (where  $u_0$  is the impact parameter in terms of the angular Einstein radius,  $\theta_E$ ; e.g. Gould 1996), or by the full width at half-maximum,  $t_{\text{FWHM}}$ . Without knowing the baseline flux coming from the lensed star, confident detection of FFPs is difficult.

K2, the ‘second-light’ mission of the *Kepler* satellite (Borucki et al. 2010; Howell et al. 2014), was pointed near Baade’s Window in the Galactic Bulge during its Campaign 9 (hereafter K2C9; Henderson et al. 2016). The area was simultaneously covered by ground-based surveys (Section 3.1). The large stellar column density predicts many detectable FFPs in this direction (Gould & Horne 2013; Ban, Kerins & Robin 2016). If the FFP population follows a distribution like Sumi et al. (2011), several (1.1–6.3) events due to FFPs were expected to be detectable (Penny et al. 2017), otherwise we expect not to observe any FFPs ( $<1$  events) during the K2C9 campaign.

To date, there has been no attempt to blindly search for short-time-scale events in the K2C9 data. Since,  $R_E$  for FFPs may be  $\ll 1$  au (cf. the 0.1–0.8 au separation between Earth and *Kelper*; Henderson et al. 2016), ground-based observations of K2C9 events may obtain very different magnifications to K2. Events detectable from one may not be detectable by the other, the microlensing parallax effect can be measured for FFP events (see e.g. Penny et al. 2017, figs 2 and 3), and the degeneracy broken between  $v_{\text{rel}}$  and  $\theta_E$  to better define the mass of the lensing object.

This paper details our blind search. Section 2 describes light-curve<sup>1</sup> extraction from the K2C9 data. In Section 3, we flag known candidate microlensing events, providing a control sample for our selection criteria. Sections 4–8 detail our selection pipeline. In Section 8.4, we present the list of known lensing events that pass through our pipeline and in Section 9 we present our final list of new candidate short-duration ( $t_{\text{eff}} \ll 2$  d) events. In Section 10, we cross-match our new candidates with photometry from ground-based telescopes. Section 11 summarizes the properties of our new events and in Section 12 we present our conclusions.

## 2 LIGHT-CURVE EXTRACTION

### 2.1 Data composition

Calibrated images for the K2C9 campaign were downloaded from the Mikulski Archive for Space Telescopes.<sup>2</sup> The observations divide into two sub-campaigns: C9a contains 1290 epochs, with a regular cadence of 30 min, between JD 2 457 501.10 and 2 457 527.44 (2016 April 22 to 2016 May 18), while C9b contains 2022 epochs between JD 2 457 531.32 and 2 457 572.44 (2016 May 22 to 2016 July 2).

Data-transfer rates meant it was only possible to retrieve a subset of the observed data. This was split between ‘postage stamps’ on known microlensing events (changed between C9a and C9b), and a much larger ‘superstamp’ which, as an unbiased data set, we analyse here. Located in the high-stellar-density Baade’s Window region of the inner Galaxy, this superstamp experiences a high rate of short-time-scale microlensing events. It comprises roughly  $3.7 \text{ deg}^2$ , centred around  $\alpha = 18^{\text{h}}$ ,  $\delta = -28 \text{ deg}$  ( $l = 2.0 \text{ deg}$ ,  $b = -2.3 \text{ deg}$ ; Henderson et al. 2016), and includes 3060 000 pixels. Fig. 1 shows the spatial extent of the observed field.

<sup>1</sup>In this work, we use *peaks* to represent any period of brightening within a specific light curve, *light curves* to represent a time-series of brightness at a given gridded sky location, and *events* to represent one or more gridded light curves exhibiting a peak at the same time. Thus, one event can be registered in many light curves, and each light curve can contain many peaks.

<sup>2</sup><https://archive.stsci.edu/k2/>

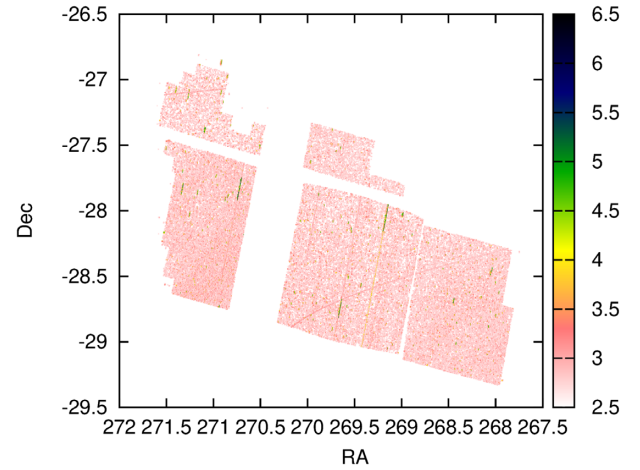


**Figure 1.** Results of initial matched filtering, showing filtered power compared to a Paczynski function with  $t_E = 7.6$  h and  $u_0 = 0$ . Red colours show events with weak power; blue colours show stronger power. Diagonal stripes from saturated stars and curved trails from asteroid tracks are visible.

Extracting precise light curves from the K2C9 data is not trivial. K2’s pointing was unstable, having lost two of its four reaction wheels. K2 was not designed for precision photometry at such high stellar densities: the large pixel scale (4 arcsec) leads to an extremely crowded field. The point-spread function (PSF) is undersampled, and strong intra-pixel variations exist. Both the PSF and intra-pixel response are wavelength-dependent, giving a very complex pixel-response function (PRF) across the broad wavelength response ( $\sim 450\text{--}900$  nm) of the *Kepler* detectors (Bryson et al. 2010; Vorobiev et al. 2018). Light-curve extraction therefore depends sensitively on the properties of individual pixels, and on the sub-pixel spatial location of stars and objects blended with them.

### 2.2 Light-curve extraction

Various techniques have used to overcome these issues (e.g. Libralato et al. 2016; Zhu et al. 2017). In less-crowded sky areas, the Causal Pixel Model (Wang et al. 2016) can remove instrumental trends and spacecraft motion from a subset of pixels, based on a training pixel set. The latter is assumed to have a constant baseline flux, but in K2C9 there are multiple stars in every pixel, each drifting in and out of pixels as the telescope moves. Consequently, we use the modified method of Poleski et al. (2019), MCPM, which was developed to work with K2C9 data and mitigates, in part, some of these effects.

Spacecraft motion means there is no one-to-one correspondence between physical detector pixels and the sky co-ordinates, as tracked by MCPM. We therefore extract a grid of light curves in right ascension and declination. Grid points were spaced uniformly at  $\Delta\delta = 3.6$  arcsec in declination and  $\Delta\alpha = 3.6 \text{ arcsec} \cos \delta$  (which is 3.14–3.21 arcsec) in right ascension, ensuring a grid spacing finer than the 4 arcsec pixel scale.

Through experimentation on known events, variable stars, stars near variable stars, and a sample of field stars, we identified a set of suitable input parameters for MCPM. We extract a light curve across six target pixels ( $n_{\text{select}} = 6$ ): this balances the extraction of most of the PSF, allowing recovery of faint candidates, with the chances of blending by bright stars. As almost every object has a known variable star within its six-pixel PSF, we use a large (400-pixel) predictor matrix, with the 10 pixels with the largest residual

**Table 1.** Extracted light curve regions. Dates are JD – 2457 000.

Region	Extracted dates	Training epochs	
C9a1	501.10–509.87	501.10–502.09	518.66–527.44
C9a2	509.87–518.66	501.10–507.68	520.85–527.44
C9a3	518.66–527.44	501.10–509.87	526.44–527.44
C9b1	531.32–544.90	531.32–532.13	558.67–572.44
C9b2	544.90–558.67	531.32–541.46	562.11–572.44
C9b3	558.67–572.44	531.32–544.90	571.44–572.44

fluxes removed. This reduces effects of nearby variable sources. The L2-regularization factor was set to  $6000 \text{ pixel}^{-1}$ .

A critical issue with this data-reduction process is that the extracted light curve depends on a training set given to MCPM. This training set assumes a prior photometric model, which we initially take as a flat light curve. At each gridpoint, MCPM extracted the light curve in six steps, each extracting one-third of the light curve for each sub-campaign. Nominally, the training set for each step bookends the extracted set of epochs, but this is not possible at the start and end of each sub-campaign (C9a and C9b). For these situations, the first or last day of the sub-campaign observations is used as appropriate. Thus, events at the very start or end of each sub-campaign will not be well recovered, however we would not accept partial light curves of events as microlensing candidates anyway. Table 1 contains a full list of Julian Dates for the extracted regions and training epochs.

This extraction is computationally expensive ( $\sim 45$  CPU seconds per light curve,  $\sim 6$  CPU years for the entire field). A total of 3752 653 light curves were extracted across all 3312 epochs, totalling  $\sim 12.4$  billion individual measurements.

### 2.3 Light-curve filtering

The six sections of the light curve were joined in temporal order, using the average flux for the 24-h period that overlaps between each section. This may reduce sensitivity to short-time-scale microlensing events occurring during these periods, and longer-term microlensing events spanning these periods. However, for this trade-off, we obtain a much-reduced amplitude of low-frequency noise.

The light curve is then high-pass filtered to further reduce low-frequency noise, using a Gaussian kernel with a 5-d characteristic width. This reduces sensitivity to long-time-scale events, but should retain FFPs signals, as they have time-scales of  $< 2$  d. This will also affect our ability to separate FFPs from bound planets on wide orbits: if the lensing star is at too high a  $u_0$ , it will produce negligible magnification to the light curve, but an orbiting planet may still provide strong magnification, resulting in an observation with two unequal components. This is a common problem in the search for FFPs. However, with our low-frequency noise filtering, the stellar signal will be smoothed out, and a bound planet may be interpreted as free floating.

Filtering also affects measures of  $t_E$ . Consequently, for the majority of this analysis we use either  $t_{\text{eff}}$  or  $t_{\text{FWHM}}$  (the full width at half-maximum flux of the differential light curve), as appropriate.

## 3 INITIAL EVENT IDENTIFICATION

### 3.1 Visual inspection of known events

Reduction of this complex data set requires an ad hoc approach candidate selection and filtering. Our design optimizes removal of false positives, while retaining light curves of the Optical Grav-

itational Lensing Experiment (OGLE-IV; Udalski, Szymański & Szymański 2015a) microlensing alerts (Udalski 2003).<sup>3</sup> We reserve events from the Korea Microlensing Telescope Network (KMTNet; Kim et al. 2016)<sup>4</sup> published by Kim et al. (2018b) to blindly test the model’s ability to reproduce new candidates. During the analysis of K2C9, additional events were announced on KMTNet website<sup>5</sup> and labelled as ‘possible’ events. Notably for this project, these include KMT-2016-BLG-2554 and -2583. For the purposes of chronological consistency, these are not considered as KMTNet detections until Section 8.4, when we identified them as candidates in the K2 data set, and totals up until that point do not discuss them except when mentioned explicitly. Events from the Microlensing Observations in Astrophysics (MOA; Sumi et al. 2013)<sup>6</sup> survey were scrutinized for events within the K2C9 superstamp, but there are no short-time-scale MOA events during the observations that are not already found by OGLE or KMTNet.

Of the 1927 microlensing alerts during the OGLE-IV 2016 campaign, few are both short and occur during K2C9. We test our pipeline on events fulfilling three criteria: (1) they peak during the K2C9 observations, (2) they have  $t_E < 4$  d (a highly conservative limit for FFPs, allowing the inclusion of brown dwarfs and FFPs with low  $\mu$ ), and (3) they occur within the K2C9 superstamp. Visual inspection of the K2C9 light curves shows that OGLE-2016-BLG-0814 is too complex to expect automatic interpretation as a single-lens, single-source event. A further three (-1041, -1058, and -1110) could not be expected to be recognized by eye without *a priori* knowledge, and two (-1097 and -1162) are only faintly visible and consistent with sporadic noise. Hence, only five light curves are expected to be detected (OGLE-2016-BLG-0813, -0878, -1043, -1231, and -1245). We track these, plus events with  $t_{\text{eff}}$  up to 10 d, through the false-positive rejection process, to minimize deselection of real candidates.<sup>7</sup>

The set of 265 KMTNet events partially overlap with OGLE-IV. Of these, 40 have modelled  $t_{\text{eff}} < 4$  d, with many  $t_{\text{eff}}$  substantially differing from the  $t_E$  of their OGLE counterparts. Of these 40, only 30 were visible in the light curves, and only 22 have sufficient noise contrast that a by-eye search would have identified them as microlensing events. One (KMT-2016-BLG-0240) peaks outside the K2C9 coverage, reducing our expected set of detected candidates numbers only 21.

Note that the  $t_E$  and  $t_{\text{eff}}$  of both OGLE and KMTNet alert systems should be used with caution: they often cannot be measured accurately because of degeneracy with  $u_0$  and/or blended flux. To circumvent this, the results by OGLE sometimes assume no blending flux, and KMTNet assumes that  $u_0$  is either zero or unity (Udalski et al. 2003; Kim et al. 2018a).

### 3.2 Basic matched filtering

Matched filtering (e.g. Helstrom & Wilson 1970) is commonly used to detect template functions in noisy datasets. A simple matched-filter analysis was performed on every light curve to obtain a first glance at the false-positive characteristics of the data set. Our chosen filter

<sup>3</sup><http://ogle.astrouw.edu.pl/ogle4/ews/2016/ews.html>.

<sup>4</sup><http://kmtnet.kasi.re.kr/~ulens/event/2016k2/>

<sup>5</sup><http://kmtnet.kasi.re.kr/~ulens/event/2016/>

<sup>6</sup><http://iral2.ess.sci.osaka-u.ac.jp/~moa/anomaly/2016/>

<sup>7</sup>Note that this set includes OGLE-2016-BLG-0559. This shows two components: one long, faint event, and one short, bright event (cf. Section 2.3). The bright event is modelled by OGLE’s Early Warning System as having  $t_{\text{eff}} = 8.2$  d, thus meets our criteria for inclusion.

is a Paczyński (1986) function, defined as the magnification factor ( $A$ ) expected from a point source undergoing gravitational lensing, as a function of time ( $t$ ), namely

$$A(t) = \frac{u^2 + 2}{u\sqrt{u^2 + 4}}, \quad (1)$$

where  $u$  is the angular displacement in angular Einstein radii ( $\theta_E$ ) of the lens from the line of sight to the source with minimum  $u_0$  occurring at  $t_0$ :

$$u = \sqrt{\left(\frac{t - t_0}{t_E}\right)^2 + u_0^2}. \quad (2)$$

For this initial analysis, we ignore stellar blending.

Each template Paczynski function was first smoothed by a 5-d Gaussian kernel and normalized to an integral of unity, to ensure consistency with the pre-processing of the observations. A variety of  $t_E$  and  $u_0$  were tested.

Fig. 1 maps the results of the  $t_E = 10^{-0.5}$  d,  $u_0 = 0$  case,<sup>8</sup> which typifies a close approach to a source star by an FFP of moderate mass. Time-integrated power in each light curve is shown in units of flux (electrons per second,  $e^- s^{-1}$ ) times time (exposures). Fig. 1 shows only events with  $>500 e^- s^{-1}$  exposures (i.e.  $\gtrsim 900\,000 e^-$ ) in total differential flux. Most fall into three categories: (1) diagonal, straight lines corresponding to charge-transfer ‘bleeding’ along detector columns from saturated stars; (2) curved tracks, from passing asteroids; (3) randomly distributed point sources, from a combination of transient events and variable stars. While instructive, these complexities mean we cannot take this matched-filtering approach further at this point, so we return to a more fundamental approach to the data analysis.

### 3.3 Automated event identification

The complexities of light-curve extraction, close mimicry of false positives, and lack of a robust training set, mean that typical ‘big data’ tools (e.g. machine learning) are not suitable for detecting microlensing events in this data. However, the data set’s size requires a comparatively simple solution. Our adopted solution combines pre-filtering and pre-whitening of the data with a generalized analysis to detect peaks in the light curves.

*Cosmic-ray pre-filtering:* Early removal of photometric spikes caused by cosmic rays led to better recovery of the OGLE test cases. To detect these, the original light curve ( $F_0$ ) was convolved with a five-point Hanning function ( $H_5$ ) and differenced from the original light curve. The median absolute deviation (MAD) of this differenced light curve was calculated, and any noise spikes  $>14.826$  MADs were removed.<sup>9</sup> Mathematically expressed, this removes any points where

$$F_0 > F_0 * H_5 + 14.286 \text{ MAD} (F_0 * H_5). \quad (3)$$

Numerically, this is similar to a very mild low-pass filter, but offers a hard cut that prevents downweighting of all but the shortest-time-scale microlensing peaks. These ultra-short-time-scale ( $t_{\text{FWHM}} \lesssim 1$  h) events should be rare, due to finite-source effects.

*Pre-whitening:* Long-time-scale variations (‘red noise’) have various astrophysical and artificial causes. Here, they appear dominated

<sup>8</sup>The model is quantized, so the singularity at  $u = 0$  is not encountered.

<sup>9</sup>The PYTHON `scipy.stats.mad` function was used for this calculation, which employs an automatic scaling factor of 1.4826. Hence, this corresponds to a function result  $>10$ .

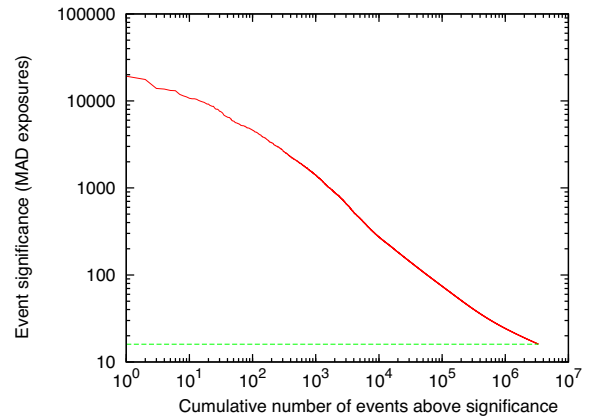


**Figure 2.** Distribution of significance ( $s$ ) among the light curves from our initial selection. The horizontal line marks our search limit.

by small-amplitude rotational and pulsational variable stars. To remove these, we now perform a high-pass filter, subtracting a Gaussian-smoothed light curve of characteristic width 2 d. This reduces our sensitivity to events with time-scales  $>2$  d, but time-scales for FFPs are normally much shorter (e.g. Mróz et al. 2017).

*Peak identification:* The light curve was then scanned for zero-flux-crossing events, between which occur either relative brightening (if positive) or dimming (if negative) compared to the baseline flux. Time-integrated flux in these regions was summed, and significance ( $s$ , in multiples of MAD over all exposures) calculated. Peaks were accepted if: (1)  $s > 16$  MAD exposures, and (2) the peak flux is ranked among the highest 5 per cent of measurements in that light curve.

This process should robustly detect any abnormal brightening of a star, identifying a large number of peaks that can be filtered to recover viable events. Within 3752 653 initial light curves, 3352 900 peaks pass this filter. The distribution of  $s$  over these peaks is shown in Fig. 2.

We compared the extracted events to the known lensing candidates, accepting a match at the position and within  $\pm 5$  d as a correctly recovered candidate. This initial stage of filtering matches all five expected OGLE events, plus the faint events OGLE-2016-BLG-1097 and -1058, and 13 of the 19 KMTNet events. The six missed events include KMT-2016-BLG-0180, the complex binary light curve; -0231, which occurs at the start of the observations; -0019 and -0024, which suffer contamination by nearby variables; and -0005 and -0068, which suffer from time-dependent noise. Thus, many known events are already missing due to blending.

## 4 RE-WEIGHTING FOR RECURRENT FALSE POSITIVES

### 4.1 Overview

The vast majority of remaining peaks are clearly not microlensing, and must be rejected by a series of cuts, outlined in Fig. 3 and subsequent sections. To deal with false positives, we first adopted a series of weights, based on the likelihood they belonged to each of these criteria. This involved identifying large-scale structures, counting the number of events per spatial co-ordinate ( $n_{\alpha\delta}$ , flagging persistent effects from saturated or variable stars), and per exposure ( $n_t$ , flagging ‘glitches’, including spacecraft repointing).

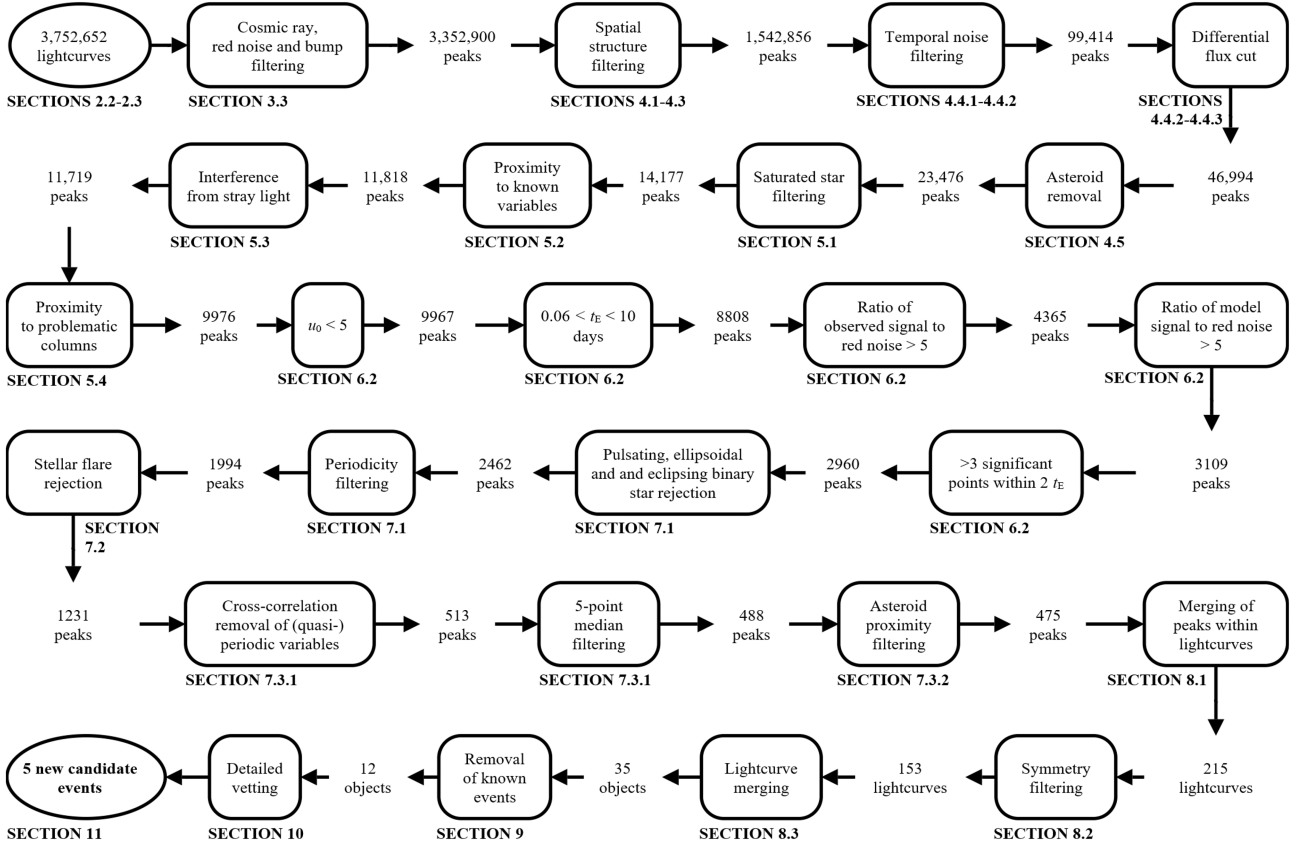


**Figure 3.** Flow diagram, showing the progressive rejection of individual peaks, light curves, and events, with corresponding section numbers.

## 4.2 Correlated structure identification

The Einstein radii of microlensing events are orders of magnitude smaller than the telescope PSF, therefore events larger than the PSF will be false positives. To detect coherent spatial structure among surviving peaks, single-linkage clustering in right ascension, declination, and time was applied to the data. Single-linkage clustering is optimally successful at identifying long clusters of objects, e.g. both long-term variability and asteroids. Variable stars with periods of  $P \lesssim 2$  d can also be isolated using this method, showing up spatially correlated events.

The SCIPY package FCLUSTER was used to perform the clustering, with a characteristic distance of 4 arcsec. A factor of 1.8 arcsec per hour ( $\sim 1$  arcsec per exposure) was used to normalize the time axis, the speed of a slow-moving asteroid. Light curves were processed in spatial chunks of  $15 \text{ arcmin} \times 15 \text{ arcmin}$  to make the process less memory intensive. The MAD of each cluster's points was calculated in each axis ( $r_\alpha$ ,  $r_\delta$ , and  $r_t$  for RA, declination, and time, respectively), and combined to give a characteristic size of the cluster:

$$r_{cl} = \sqrt{\left(\frac{r_\alpha}{\cos \delta}\right)^2 + r_\delta^2 + \left(\frac{r_t}{1.8 \text{ arcsec h}^{-1}}\right)^2}. \quad (4)$$

Fig. 4 shows those structures with sizes (or size-normalized times) greater than 0.01, clearly showing many asteroid trails (curved lines in both panels) and variable stars (vertical lines in bottom panel).

## 4.3 Light-curve weighting

Next, we generated weights for each peak based on their cluster extent ( $w_{cl}$ ), and frequency in space ( $w_{\alpha\delta}$ ) and time ( $w_t$ ). The weighted

significance for each light curve ( $s_w$ ) is given by

$$s_w = s w_{cl} w_{\alpha\delta} w_t. \quad (5)$$

Each weight is based on a Gaussian cumulative distribution functions  $\text{CDF}(d; c, \sigma)$ , for observed value  $d$ , mean  $c$ , and scale  $\sigma$ , softly cutting off large clusters, positions, or times:

$$\begin{aligned} w_{cl} &= 1 - \text{CDF}(r_{cl}; 0.01, 0.005), \\ w_{\alpha\delta} &= 1 - \text{CDF}(\log_{10} n_{\alpha\delta}; 1.3, 0.3), \text{ and} \\ w_t &= 1 - \text{CDF}(\log_{10} n_t; 2.8, 0.2). \end{aligned} \quad (6)$$

The mean and scale of each distribution was chosen a posteriori based on visual inspection of the retained/rejected peaks and their distribution. These cuts are conservative, minimizing false negatives. Only peaks with  $s_w > 16$  were retained, reducing the 3352 900 peaks to 1542 856. All detected OGLE and KMTNet candidates passed this cut.

## 4.4 Saturated and blended stars

### 4.4.1 Column bleeding

Despite this weighting, visual inspection shows a significant fraction of bright peaks arise from trails from bright, saturated stars that leave sporadic brightening patterns as charge bleeds down the CCD columns. Affected positions change as stars move between and within pixels on the detector, and as the spacecraft rotates. These effects are coherent in time. To address this, we computed two additional weights.

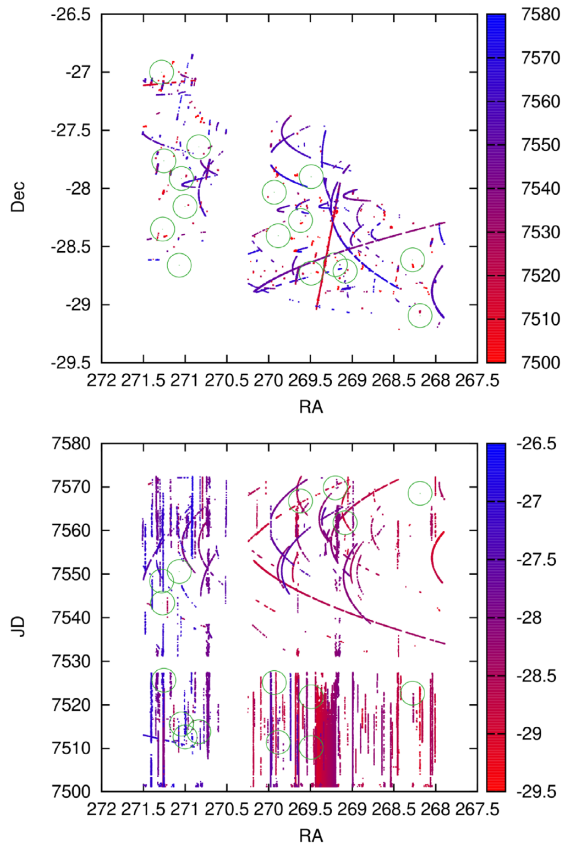


**Figure 4.** Large-scale or temporally repeating structures filtered by single-linkage clustering. Circles indicate OGLE events. Colours represent Julian Date and declination for top and bottom panels, respectively.

The first weight targets structures aligned with detector columns. Peaks were binned along the detector axis ( $\sim 12^\circ 2$  rotation west of north) in  $3.6 \text{ arcsec} \times 2 \text{ h}$  bins, and a weight,  $w_{\text{col}}$ , was assigned based on the number of peaks in that bin ( $n_{\text{col}}$ ) following

$$w_{\text{col}}(t) = 1 - \text{CDF}(n_{\text{col}}; 30, 10). \quad (7)$$

#### 4.4.2 Temporally correlated noise

In addition, many physically isolated but temporally coincident peaks remain. *Kepler*'s undersampled PSF means that flux from individual stars is distributed over a small number of pixels. When combined with the undersampled PSF, the high stellar density, and significant spatial differences in sensitivity within each pixel, the blended flux from nearby bright stars can vary significantly as the spacecraft pointing drifts. Such cases appear to represent the vast majority of false positives remaining in the data set.

Therefore, we used the normalized number of peaks per exposure ( $n_t$ ) to define a pure noise ‘light curve’:

$$f_{\text{noise}}(t) = \frac{1 + n_t(t)}{1 + n_t^{\text{max}}}, \quad (8)$$

where  $n_t^{\text{max}}$  is the exposure with the most peaks. The top panel of Fig. 5 shows the resulting pure-noise light curve, indicating most peaks fall within a few specific time bins.

Peaks were further smoothed by an aggressive Gaussian high-pass filter ( $\sigma = 0.4 \text{ d}$ ), removing structures not associated with noise peaks. The heavily smoothed light curves ( $f_{\text{sm}}$ ) were compared to the

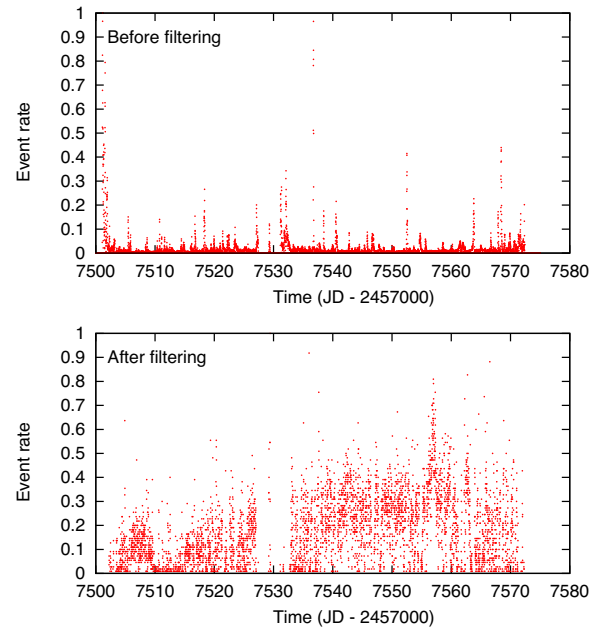


**Figure 5.** Relative rate of K2C9 peaks before and after filtering. The top panel is used as a noise template ( $f_{\text{noise}}$ ) to downweight and remove peaks, resulting in the bottom panel. The spike near JD 2457 557.6 is from an unplanned 20 arcsec roll offset, and reversal of the telescope drift rate due to solar radiation pressure.

pure-noise light curve, and the ratio of ‘noise-’ to ‘signal-like’ flux calculated over all exposures ( $t$ ) using

$$R_{\text{noise}} = \sum_t \frac{f_{\text{noise}}(t)f_{\text{sm}}(t)}{f_{\text{noise}}(t)(1 - f_{\text{sm}}(t))}. \quad (9)$$

Hence, large  $R_{\text{noise}}$  indicates events associated with blended stars and spacecraft motion, whereas small  $R_{\text{noise}}$  indicates a potential event. The mean  $R_{\text{noise}}$  is 0.0321 and standard deviation is 0.0096. To retain real events (including those scattered by noise up to  $\sim$ one standard deviation), we create a weight,  $w_{\text{noise}}$  that downweights noise-like signals:

$$w_{\text{noise}} = 1 - \text{CDF}(R_{\text{noise}}, 0.0321 + 0.0096, 0.0096), \quad (10)$$

and create a new significance,  $s'_w$ , such that

$$s'_w = s_w w_{\text{col}} w_{\text{noise}}. \quad (11)$$

Again, peaks with  $s'_w > 16$  were kept, reducing 1542 856 peaks to 99 414. Their temporal and spatial distribution after filtering are shown in Figs 5 (bottom panel) and 6.

One OGLE candidate (-0878) was partially lost during this cut: its grid point was flagged as correlated noise. However, a neighbouring grid point remained. Five KMTNet candidates were lost (-0051, -0134, -0155, -0206, and -0209) and KMT-2016-BLG-0151 was partially lost. Of these, -0151, -0134, -0151, and -0155 have longer time-scales ( $\sim 4\text{--}6 \text{ d}$ ) in OGLE and, if such time-scale are accurate, would not be expected to survive the vetting process. The two remaining KMTNet candidates (-0206 and -0209) were not detected by OGLE.

#### 4.4.3 Differential flux weighting

Many remaining peaks have substantial jitter in their wider light curves, as the photocentres of bright stars move in and out of the targeted pixels when the spacecraft moves. While many were

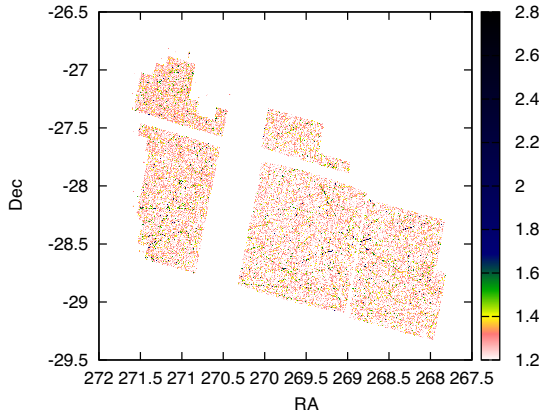


**Figure 6.** Distribution of peaks after weighting. Colours are as in Fig. 1.

**Table 2.** Regions searched for asteroids.

RA	Dec.	Radius
17 53 20.00	-28 45 00	40 arcmin
17 58 00.00	-28 00 00	1°
18 04 00.00	-27 48 00	1°

caught by the  $s'_w > 16$  cut, some remain. They are characterized by a sawtooth-shaped light curve with a time-variable amplitude, while real events should have a much smoother light curve away from the main peak.

The raw light curves were again subject to a Gaussian high-pass filter ( $\sigma = 2$  d). The standard deviation of this filtered light curve is taken, masking out event mid-point and the 2 d on either side. The masked epochs, representing the event, are then sorted in brightness and the top four epochs taken. Peaks were passed provided the flux in those four events exceeded  $5$ ,  $5/2$ ,  $5/3$ , and  $5/4$  times the standard deviation outside the event, respectively. This cut also removed spurious events where only one epoch exceeded the noise threshold, which could be due to instrumental issues, e.g. remnant cosmic rays. The total number of peaks was thus reduced from 99 414 to 46 994. All OGLE and KMTNet candidates passed this cut.

#### 4.5 Asteroid removal

Most visually obvious false positives in Fig. 6 are from asteroid trails that were not identified as long arcs.

To identify the observed asteroids, three circular apertures were set up to cover the entire K2C9 field, detailed in Table 2. The JPL/NASA ISPY service<sup>10</sup> was queried in each region between JD 2457 500 to 2457 575 in steps of 2.5 d: 1149 asteroids exceeded magnitude 21.0 during any one of these epochs. Ephemerides for each were generated in 30-min intervals using the HORIZONS service.<sup>11</sup>

The Euclidean distance of each event to each ephemeris was computed, and the closest ephemeris chosen. Events were rejected if that distance was  $< 0.07$  and the time difference was  $< 0.2$  d. *Kepler* detected 477 individual asteroids, and their removal halved the number of peaks from 46 994 to 23 476. All OGLE and KMTNet candidates passed this cut.

## 5 REGIONAL MASKING

Many remaining peaks are heavily down-weighted but exceptionally strong false positives. This section describes the techniques used to entirely mask the worst cases.

### 5.1 Bright stars

A stellar catalogue, covering the regions in Table 2, was extracted from *Gaia* Data Release 2 (*Gaia* DR2; *Gaia* Collaboration 2018), and rotated into detector co-ordinates (see Section 4.4.1).

Masks were generated around *Gaia* objects depending on their  $R_p$ -band magnitude. Three cuts were made:

(i)  $G_{Rp} < 9$  mag. Around each star, three rectangular regions were masked. The first ( $0:0025$  either side of the star, over the entire detector length) masks complete column bleeds. The second ( $\pm 0:0035 \times 0:25$ ) masks shorter bleeds from the star's extended PSF. The third ( $\pm 0:005 \times 0:05$ ) masks effects from the PSF halo.

(ii)  $9 \text{ mag} \leq G_{Rp} < 10$  mag. A single window of  $\pm 0:0035 \times 0:01$  was masked around stars of to remove shorter column bleeds.

(iii)  $10 \text{ mag} \leq G_{Rp} < 11$  mag. A single window of  $\pm 0:0025 \times 0:005$  was masked around marginally saturated stars.

While some problematic sources remain, the list of peaks was reduced from 23 476 to 14 177 events. KMT-2016-BLG-0133 and the remaining light curve associated with -0151 (OGLE-2016-BLG-0813) were removed by this mask.

### 5.2 Variable stars

A list of 61 941 variable stars was compiled, the vast majority being from the OGLE catalogue of variable stars<sup>12</sup> (Soszyński et al. 2013, 2016), with some additions from other surveys. The sensitivity of OGLE to variable stars varies over the superstamp, as the OGLE-III catalogue only covers the eastern part of the K2C9 superstamp. Overall, however, most positions in K2C9 are  $\leq 18$  arcsec from a known variable star: fully masking every variable star would also mask many chance alignments. We chose instead to mask a smaller aperture, according to three magnitude restrictions: (1) a circle of 3.6 arcsec ( $\sim 1$  *Kepler* pixel) around every variable star; (2) 7.2 arcsec around stars with  $V < 15$  or  $I < 15$  mag, or with amplitudes  $\Delta I > 1$  mag; (3) 10.8 arcsec around stars with  $V < 12$ ,  $I < 12$ , or  $\Delta I > 2$  mag. This reduced 14 177 peaks to 11 818. KMT-2016-BLG-0138 and -0149 were masked by this cut. The latter is matched to OGLE event OGLE-2016-BLG-0914, with  $t_E \approx 8$  d.

### 5.3 Stray light

A stray light event occurred towards the end of the campaign. The artefacts it created are not visible on the raw images, but show up in the differenced images as straight lines. The underlying cause was not identified, but could be related to the 'Argabrightening' events, thought to be caused by impact debris from the telescope structure (Witteborn et al. 2011). The 99 associated peaks were removed by creating a diagonal mask in the detector plane, removing peaks where  $-28.2 < \delta + (\alpha - 271.1)/1.5 < -27.7$

<sup>10</sup><https://ssd.jpl.nasa.gov/x/ispay.html>.

<sup>11</sup><https://ssd.jpl.nasa.gov/horizons.cgi>.

<sup>12</sup><http://ogledb.astrouw.edu.pl/~ogle/OCVS/>.

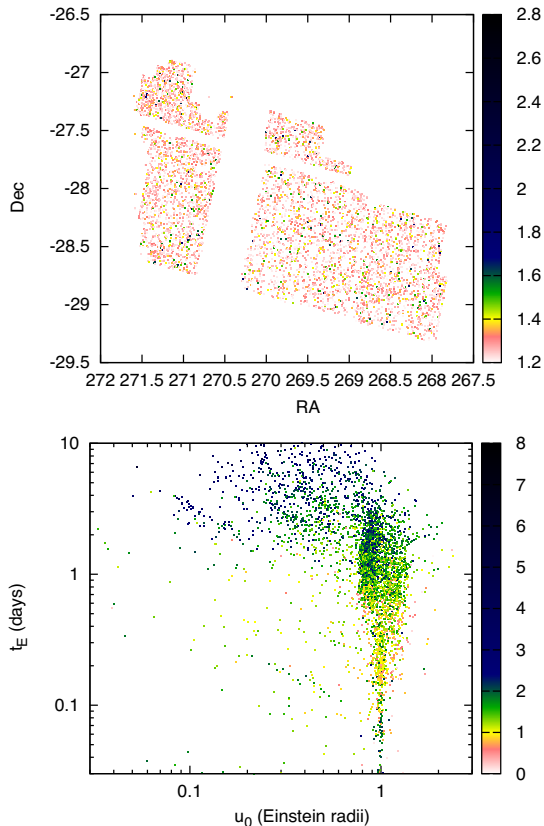


**Figure 7.** Top panel: sky locations of filtered K2C9 light curves. Colours are as in Fig. 1. Bottom panel: fitted impact parameter and Einstein-crossing time-scale for the same set of light curves, assuming them to be due to microlensing. The colour scale denotes the peak signal-to-noise (Section 6.1).

(where  $\alpha$  and  $\delta$  are the RA and Dec. in decimal degrees) and  $2457\,565.7 < \text{JD} < 2457\,565.8$ .

#### 5.4 Problematic columns

Strips were created across the detector column axis (cf. Section 4.4.1) of width  $0.001^\circ$  by 0.1 d (approximating the PSF radius and shortest recoverable event). Strips containing ten or more events were masked. This primarily affected sections of module 15, where bright the high stellar density led to additional saturation for overlapping bright stars.

A further set of columns were prone to producing false positives, but with a spread in time. To remove these, another iterator parsed the same  $0.001^\circ$ -wide regions. Regions were masked if: (1) they contained more than 10 events, (2) if the standard deviation along the row axis exceeded  $0.01^\circ$ , and (3) fewer than 40 per cent of the events fell within  $0.01^\circ$  of the median position. This retains multiple flaggings of the same event, while masking large simples of events occurring in separate locations.

This reduced the peak list to 9976 events at 8306 sky positions. The largely uniform sky distribution of these peaks can be seen in the upper panel of Fig. 7.

Following this noise rejection process, we retain only three of the expected five OGLE events (OGLE-2016-BLG-1043, -1231, and -1245) and eight of the expected 21 KMTNet events (KMT-2016-BLG-0090, -0117, -0124, -0128, -0143, -0162, -0181, and -0189). Consequently, roughly half of the events visible in the light curves do not pass our detection pipeline.

## 6 LIGHT-CURVE RE-EXTRACTION AND FITTING

### 6.1 Re-extraction

The MCPM extraction is model dependent (Section 2.2). We a priori assumed a flat light curve for each object. However, this small set of light curves can now be re-extracted, fitting a single-lens, single-source microlensing model. Accurate fitting is still impossible, as structured noise in the light curves (primarily from spacecraft motion and remaining variable stars) correlates strongly with the fitted event model. Nevertheless, a set of initial model fits can estimate the event properties, allowing further false positives to be removed. Note that we only use this re-extracted set of light curves in this section for the purposes of false-positive removal: we do not fully fit model parameters in this work.

Each peak was fitted using MULENSMODEL<sup>13</sup> (Poleski & Yee 2019), which interfaces with MCPM: we minimized the root-mean-squared residual between the model and light curve to both fit the light curve and improve the quality of the extracted photometry. We used the Nelder–Mead (downhill simplex) method of minimization. The parameters  $t_0$ ,  $u_0$ ,  $t_E$ , and  $F_{s,K2}$  (flux of the source star) were solved simultaneously. The first vertex of the simplex was initialized to the event time found by the peak finder,  $u_0 = 1 R_E$ ,  $t_E = 2$  d, and  $F_{s,K2} = 100 e^- s^{-1}$ . The subsequent four vertices were respectively adjusted to 3 d before the peak-finder time,  $u_0 = 0$ ,  $t_E = 0.2$  d, and  $F_{s,K2} = 1000 e^- s^{-1}$ . The MCPM minimizer tolerance was set to 0.0001. Only the sub-campaign (C9a or C9b) in which the event occurred was re-extracted. The bottom panel of Fig. 7 shows the  $u_0$  and  $t_E$  extracted for each event. We remind the reader of the strong degeneracies between these parameters, particularly  $F_{s,K2}$  and  $t_E$ . Consequently, these values are not to be taken as direct parametric measures, but merely as an aid to candidate selection in the next section.

Many models were poorly fit, normally because the extracted signal did not resemble a microlensing event. These events result in the vertical stripe in Fig. 7 around  $u_0 = 1 R_E$ . Real events are typically represented by many neighbouring spatial gridpoints, and scatter in diagonal lines towards lower  $u_0$ , highlighting the degeneracy between extracted  $t_E$  and  $u_0$  in the fitting procedure.

### 6.2 Noise filtering

The improved photometry and the fitted model allow better separation of false positives using the event’s signal-to-noise ratio. To re-evaluate the light-curve noise, we first perform the same 2-d Gaussian filtering as previously, retaining both the low- and high-pass filtered components to (respectively) represent the temporally correlated (‘red’) and uncorrelated (‘white’) noise in the light curve.

Epochs outside the range  $t_0 \pm 2t_E$  were used<sup>14</sup> to generate out-of-event noise amplitude for each component, determined as half the difference between the 5th and 95th centile fluxes over these out-of-event epochs. A median (50th centile) out-of-event flux was also established. The amplitude of the model, and the peak-to-median difference in observed flux were (respectively) used to derive two signal amplitudes: one for the model and one for the observed data.

A good candidate should have realistic fitted parameters and a peak substantially exceeding both the light curve’s correlated and uncorrelated noise. Consequently, we remove peaks that do not fit

<sup>13</sup><https://github.com/rpoleski/MulensModel>

<sup>14</sup>Note the caveats in Section 6.1 regarding use of  $t_E$ .

all of the following criteria.

(i)  $u_0 < 5R_E$ . Peaks with larger  $u_0$  will not produce significant magnification and are likely to be poorly fit models. This removes nine peaks.

(ii)  $t_E < 10$  d. Long-time-scale peaks will not be FFPs. This cut corrects an issue from the above noise calculation, when no epochs exist to estimate noise from when  $t_E$  is large. This removes 353 peaks.

(iii)  $t_E > 0.06$  d. Extremely short-time-scale peaks are indistinguishable from artefacts or other short transients, and the existence of finite-source effects in true FFPs (i.e. it takes a finite time for the Einstein ring of the lens to cross the source's stellar disc) mean extremely short events are unlikely to have an origin in an FFP lensing event (cf. Mroz et al. 2020). This removes 300 peaks.

(iv) A ratio between the observed signal strength (time-integrated flux within  $t_0 \pm 2t_E$ ) and the red noise that exceeds 5. This removes 506 peaks.

(v) A ratio between the model signal strength and the red noise that exceeds 5. This removes 4443 peaks.

(vi) A ratio between the observed signal strength and the white noise that exceeds 5. This removes 1256 peaks.

(vii) More than three photometric datapoints within  $2 t_E$  of the fitted event centre that are above the 99th centile in both the original (flat-prior) and re-extracted (fitted-lens-prior) light curve. This removes 149 peaks.

Our peaks thus reduce from 9976 to 2960, occurring at 2229 sky positions. Single-linkage clustering suggests these represent  $\sim 1770$  discrete events. All remaining known events passed this cut. Visual inspection of these peaks shows that, while some data artefacts are still present, most remaining peaks appear astrophysical in nature.

## 7 DETAILED CANDIDATE SELECTION

In this section, we continue to use automated cuts to remove false positives. However, each rejected peak is first subject to individual visual scrutiny. Peaks in light curves including suspected microlensing events are only rejected if other detections of the same event occur at the same sky position.

### 7.1 Variable star filters

Many remaining peaks are pulsating or ellipsoidal variable stars. In the flat-prior light curve, the complex PRF changes the amplitude of variability as the spacecraft moves, making some peaks stronger than others. MULENSMODEL then interprets strong peaks as microlensing events and, if the modelled blending fraction is high, an unreasonably high amplitude will be returned. A set of sequential filters remove these variables.

Such stars have light curves that are largely symmetrical around zero flux. Events were rejected if the lowest point on the original (flat-prior) light curve (Section 2) is  $>7.5$  times lower than the 16th centile of the light curve. Events were also rejected by comparing the faintest 0.2 centile (second permille) against the brightest (998th permille): if the second permille is further below the mean than the 998th permille is above the mean, the light curve is characterized better by dips than brightenings, triggering rejection. These cuts were quite effective, leaving 2462 peaks at 1822 sky positions.

The dominant frequency of each light curve was identified using a Lomb–Scargle periodogram of the flat-prior light curve, over the period range 0.1–10 d. A Ricker wavelet at this frequency was used

as a matched filter on the light curve. Peaks were kept if they met both the following criteria: (1) that the ratio of the maximum of the cross-correlation function (CCF) within  $t_0 \pm t_E$  to the maximum outside this range was  $< \sqrt{N_p}$ , where  $N_p$  is the simple of period cycles over the entire light curve (thus filtering strongly repeating variables); and (2), that the dominant period is less than half the fitted  $t_E$  (thus retaining short, spike-like events).

Our final filter uses the amplitude of the CCF as a smoothed light curve. When subtracted from the flat-prior light curve, this creates a high-pass filtered light curve. The ratio of the absolute sum of the residuals of this filtered light curve to that the original light curve effectively provides the mean amplitude of the residual light curve after subtracting power at the strongest frequency. Peaks were rejected if the ratio in the sub-campaign during which the peak signal *did not* occur was  $<0.7$ , i.e. if a single sinusoid represents  $>30$  per cent of the differential light curve. These cuts were effective at removing many pulsating stars, including many that appear to be rotationally modulated flare stars. The cuts leave 1994 peaks at 1433 sky positions.

### 7.2 Flare filters

Noise spikes now dominate the false positives, most being stellar flares on late-type dwarf stars, often identifiable as rotationally modulated variables with one or more sudden spikes in flux. These can be difficult to separate from very-short-time-scale microlensing events. However, while microlensing events are symmetrical, stellar flares are skewed, brightening suddenly, then fading over a few exposures.

We fitted a skewed Gaussian to each peak with the SCIPY statistics package SKEWNORM via  $\chi^2$  minimization. A central time-scale ( $t_{0,skew}$ ), amplitude, width ( $\sigma_{skew}$ ), and skew parameter ( $a_{skew}$ ) were fit. Sources were rejected if any of the following criteria were met:

(i)  $a_{skew} > 4$ , provided  $t_{0,skew}$  was within  $\sigma_{skew} + 0.2$  d of the initially flagged event (to avoid fitting other events that are already rejected);

(ii)  $\sigma_{skew} < 0.02$  d, as these are universally single-epoch noise spikes (e.g. associated with cosmic ray hits);

(iii)  $\sigma_{skew} > 2$  d: FFP events should be shorter, and all such events exhibit sinusoidal variability;

(iv) sources with negative amplitudes, as these are also associated with variable stars;

(v) events peaking outside the observing window, or within 1 d of the start or end of a sub-campaign, and all such events are simply long-term photometric trends.

These cuts leave 1231 peaks at 898 sky positions.

### 7.3 More variable star filters

#### 7.3.1 Peak significance filtering

Many peaks are still due to variable stars or sporadic noise spikes. Most have not yet been removed because the fitting functions have improperly characterized the event time-scale. This is often because of multimode pulsations or correlated noise related to spacecraft motion.

To better characterize the time-scale, a fixed  $t_0$  was assumed, and a window of  $\pm 0.25$  d selected around the peak. The average absolute deviation in the event ( $\Gamma_{in}$ ) was calculated, and divided by the average absolute deviation in the remainder of the light curve ( $\Gamma_{out}$ ). The windowing function was increased in increments

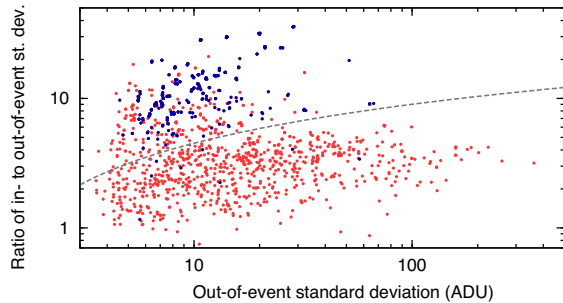


**Figure 8.** The relative signal-to-noise in a window around the peak, compared to the remainder of the light curve (Section 7.3.1). Darker, blue points mark known events; lighter, red points mark surviving peaks. Peaks below the dashed line are rejected. Known events below the line occur at different times from the event itself.

of 0.01 d, up to 2 d, and the time-scale with the maximum ratio of  $\Gamma_{\text{in}}/\Gamma_{\text{out}}$  was chosen. This function is robust against events of different shapes.

Fig. 8 shows this maximized ratio as a function of the corresponding  $\Gamma_{\text{out}}$ . The dotted line largely separates potential candidates from false positives, and is derived as

$$\Gamma_{\text{in}}/\Gamma_{\text{out}} = 4.5 \log_{10} \Gamma_{\text{out}}. \quad (12)$$

The increase in this ratio with  $\Gamma_{\text{out}}$  is motivated by the tendency for light curves with large  $\Gamma_{\text{out}}$  to be more greatly affected by correlated instrumental noise or pulsations of variable amplitude, rather than by random processes.

This cut is both efficient and severe (removing 718 peaks, leaving 513), hence it is performed at this late stage to allow visual confirmation: known false negatives (events spatially near microlensing sources) display a markedly different  $t_0$  to the known event, and often very differently shaped light curves. Visual inspection also highlighted five rejected events that passed visual inspection for microlensing events. Of these, two ( $\alpha = 268.473$ ,  $\delta = -28.914$ ,  $t_0 = 7516.93$  and  $\alpha = 268.183$ ,  $\delta = -28.782$ ,  $t_0 = 7519.67$ ) are visually noticeable but comparatively faint; another ( $\alpha = 268.090$ ,  $\delta = -27.341$ ,  $t_0 = 7522.93$ ) appears good, but the light curve suffers from correlated noise, modulated on a similar time-scale to the event. The final two events are discussed in the next section.

Several of the remaining events are of poor quality, but are retained as a single exposure within the event boosts their statistical weight. Therefore, a five-point median filter was applied to each light curve and the process run again, again removing objects failing the cut-off in equation (12), or with  $\Gamma_{\text{in}}/\Gamma_{\text{out}} < 5$ . This removed an additional 25 peaks.

### 7.3.2 Additional asteroid filtering

The two remaining events discussed above were flagged at slightly different times. They occur when two asteroids pass over almost the same place at the almost same time, causing a single brightening of that spatial location. A single event was assigned, but offset in time from the ephemeris of either asteroid, hence missed by our earlier cut. Hence, we now remove any event within 0.2 and 0.5 d of an asteroid passage. This removed 13 peaks, leaving 475 peaks, of which 277 are  $<0.005$  and  $<2$  d from existing OGLE or KMTNet events. The other 198 peaks map to 97 sky positions, which clustering analysis associates with  $\sim 66$  unique events.

## 8 DETAILED EVENT SELECTION

### 8.1 Merging peaks

Multiple detections for each event arise from slightly different peaks identified in the first stage of the reduction. By now, only one physical brightening is associated with each light curve, merely flagged on multiple occasions. Hence, we can merge peaks in the same light curve together.

We first choose the peak with greatest signal in each light curve. This choice is not greatly important, as it only seeds the data reduction. We refit a skewed Gaussian to each peak using the `SCIPY.STATS.SKEWNORM` tool, but refining our previous technique as below. A Gaussian is used instead of a Paczynski function both to aid computation and because of its generalized application to non-microlensing peaks. The skew parameter is employed to fit stellar flares and outbursts.

Correlated noise (Section 4.4.2) means that a parametric fit contains many local minima, making it hard to find an accurate, global-minimum best fit. Consequently, we start with an initial Monte Carlo fit to the light curve, with initial parameters of the peak time (Section 3.3), time-scale (Section 7.3.1) and amplitude (Section 6.2), and zero skew. Over 10 000 Monte Carlo iterations, a random perturbation in the event time was chosen from a normal distribution of width 0.5 d; the event width and amplitude were each multiplied by a factor drawn from a normal distribution with a unity mean and a standard deviation of 0.25; and the skew was drawn randomly from within the range  $-4$  to  $+4$ . The fit with the lowest average squared deviation within 2 d of the supplied event time was then used as a seed for the `numpy.optimize.minimize` Powell minimization function, which was run with default parameters.

This process was repeated for each peak, and the peak with the lowest average squared deviation after minimization was selected to represent the best detection in that light curve, leaving light curves representing 215 spatial positions.

### 8.2 Symmetry filtering

The primary contaminants remain flares, and both instrumental and real step jumps in flux. The fitted Gaussian functions still have difficulty finding a global-minimum best fit, so were fitted again with 100 000 Monte Carlo iterations. This improves the fits in many cases, though some light curves are still very poorly fit.

Events were removed as stellar flares if: (1)  $|a_{\text{skew}}| > 5$  (most known microlensing events have  $|a_{\text{skew}}| < 2$ ); and (2) the fitted Gaussian better fit the overall light curve than an unchanging baseline flux; and (2) the average squared deviation from the fitted Gaussian at time-scales  $>2$  d from the event increase by no more than 1 per cent compared to the baseline flux. This ensures that only well-fitted, flare-like events were removed. This leaves light curves representing 153 sky positions, of which 85 are associated with known events.

This cut removed two known lenses that do not have Gaussian-like light curves: the binary event OGLE-2016-BLG-1043 and KMT-2016-BLG-0209. The latter event peaks  $\sim 1$  d from the start of the observations, and its beginning is not fully observed. The 1-d training set used for photometric extraction at the start of the light curve is therefore not flat, and the event is not recovered symmetrically.

Visually inspecting the rejected light curves identifies two novel events that could be microlensing events, but are more likely correlated noise and a stellar flare. These occur respectively at  $\alpha = 270.778$ ,  $\delta = -27.511$ ,  $\text{JD} = 2457\,505.34$  and  $\alpha = 271.137$ ,  $\delta = -26.920$ ,  $\text{JD} = 2457\,551.64$ .

**Table 3.** Events manually rejected as their light curves do not resemble microlensing events. Dates are JD – 2450 000.

RA	Dec.	Date	Notes
268.256	–28.417	7521.134	Flare
268.523	–28.308	7564.411	Instrumental
269.386	–28.716	7542.186	Periodic
269.619	–28.250	7555.556	Flare
269.643	–28.869	7534.066	Instrumental
269.653	–28.627	7561.789	Instrumental
269.671	–27.480	7517.815	Periodic
269.871	–27.653	7520.603	Long
270.001	–27.562	7544.414	Periodic
270.160	–28.452	7531.917	Noise
270.552	–27.397	7515.642	Flare
270.802	–28.391	7536.428	Long
270.951	–27.220	7533.143	Flare
271.068	–28.016	7535.643	Long
271.231	–27.206	7566.090	Flare
271.362	–27.059	7569.184	Long

This cut also affects binary microlensing light curves. Two out of three events were removed for an event at  $\alpha = 269.880$ ,  $\delta = -27.608$ , JD = 2457 518.89. The remaining event is discussed later. No other such events were visually detected.

### 8.3 Light-curve merging

With a near-final set of light curves, we can now perform single-linkage clustering (as in Section 4.2) to merge associated light curves at neighbouring positions into individual events. Physical events are now cleanly separated from each other in space and time, allowing easy clustering.

For each event, the position with the largest-amplitude time-integrated signal was chosen as an initial localization to represent the light curve. These positions undergo later refinement, so exact positions at this stage are not critical.

This produced 35 candidate microlensing events recovered from the K2C9 data set with  $t_{\text{FWHM}}$  consistent with an FFP, plus 22 associated with known lenses (after removing a cataclysmic variable; note we now include KMT-2016-BLG-2554 and -2583 in this list), inspected in Section 8.4. Our list of 35 candidate events are examined in Section 9.

### 8.4 Properties of known events

Full fitting of known events, combining ground-based data with K2, is deferred to future papers. Here, we use MCPM on these events a final time to formally fit  $t_0$  and  $t_{\text{eff}}$  directly from the K2C9 light curves. These fits are discussed in the online Appendix.

## 9 INSPECTION OF CANDIDATE EVENTS

### 9.1 Visual inspection

We now visually analyse the 35 objects selected for detailed inspection: the 16 listed in Table 3 are clearly associated with sporadic noise, poorly fit stellar flares, periodic variable stars, and instrumental artefacts. Most were not previously rejected because they were poorly fit by the Gaussian fitting process due to correlated noise in their light curves.

**Table 4.** Events manually rejected as they do not resemble microlensing events after recentering. Dates are JD – 2450 000.

RA	Dec.	Date	Notes
268.1453	–28.3631	7570.3924	Instrumental
268.2190	–28.8010	7567.1473	Variable/flares
268.9946	–28.5364	7525.1526	Flare
269.0820	–28.7943	7559.0575	Asteroid
269.1930	–28.2440	7551.2838	Flare
269.5045	–28.2915	7514.5276	Variable
269.7970	–27.5460	7543.8977	Flare
270.7014	–28.1039	7547.4999	Variable
270.8377	–27.3961	7541.6519	Flare
271.2873	–27.1084	7536.7764	Slow
271.3748	–27.2682	7564.3321	Noise

### 9.2 Object recentering

In this crowded field, the parameters used for the photometric extraction affect the final light curves, due to blending from nearby stars. Some candidates are both cotemporal with and within the PSF-radius of much stronger events, many of which have already been rejected. This was intentional: events must be extracted from within the PSF of variable stars, etc., so we must rely on light curves away from the PSF centre to detect subtle changes. However, we now need to recenter and re-extract these events to determine their true nature.

The flat-prior light curves within 0:003 of the candidate were windowed to the event time-scale (i.e. the Gaussian width fitted in Section 8.2). The flux-weighted means of RA, Dec., and JD of these light curves recenter the event.

The surrounding light curves were then inspected to ensure that only one event had been selected. In a few cases, this did not work correctly. One candidate ( $\alpha = 268:145$ ,  $\delta = -28:363$ ) lies on a chip boundary, while two other candidates ( $\alpha = 269:716$ ,  $\delta = -27:654$ ;  $\alpha = 269:797$ ,  $\delta = -27:546$ ) were each not correctly separated from a variable star. These positions were not updated. Another candidate ( $\alpha = 268:222$ ,  $\delta = -28:798$ ) was successfully relocated 0:004 away.

### 9.3 Re-evaluation of recentered light curves

Of the 19 remaining light curves, 11 have been recentered on non-microlensing events. Six of these events were previously rejected based on higher quality light curves from the centres of their PSFs. Five events were rejected because structure before or after the event provides evidence against a microlensing event. Table 4 lists these rejects.

In four of the six in-event cases, the increased signal-to-noise ratio clarified the event as a stellar flare. A fifth event occurs near a chip edge, and is noise associated with the unprogrammed roll and correction. The final event was generated by asteroid 2009 BQ168. While our analysis was on-going, the brightness estimated by JPL HORIZONS slightly increased: it is now expected to have brightened to marginally over 21st magnitude. This would barely warrant its inclusion in our asteroid list, but it would be undetectable. However, the recovered event is closer to magnitude 18.5 in the *Kepler* bandpass. Possible explanations include the magnitude of 2009 BQ168 being underreported (the HORIZONS magnitudes are knowingly approximate); that the asteroid is exceptionally red, hence has a ( $V - K_p$ ) colour of  $\sim 2.4$  mag; or that the asteroid may have undergone an outburst.

Three of the five out-of-event cases show clear periodicity; one shows further stellar flares in its light curve. The ‘slow’ case

**Table 5.** Fitted parameters of novel candidate microlensing systems undergoing detailed inspection.

K2C9- 2016- BLG-	K2C9 location		Fitted parameters			Final class
	RA (J2000)	Dec.	$t_0$ (JD) <sup>a</sup>	$t_{\text{eff}}$ (d)	$F_s/u_0$ ( $e^- s^{-1}$ )	
1	267.9361	−28.9215	$7511.4562^{+0.0040}_{-0.0041}$	$0.0535^{+0.0037}_{-0.0034}$	$119.5^{+4.8}_{-4.7}$	Passed, confirmed as astrophysical
2	268.6613	−28.6140	$7544.5050^{+0.0009}_{-0.0009}$	$0.0168^{+0.0009}_{-0.0008}$	$313.5^{+10.0}_{-9.6}$	Passed, unconfirmed
3	269.7156	−27.6540	$7522.9878^{+0.0059}_{-0.0061}$	$0.0616^{+0.0083}_{-0.0072}$	$75.0^{+5.5}_{-5.2}$	Passed, unconfirmed
4	269.8359	−27.5522	$7558.0645^{+0.0036}_{-0.0035}$	$0.0360^{+0.0042}_{-0.0037}$	$109.3^{+7.3}_{-7.0}$	Passed, unconfirmed
5	269.8798	−27.6074	$7518.1435^c$	$_{-b}$	$_{-b}$	Passed, confirmed as lens
—	270.9172	−27.2671	$7561.0904^c$	$0.852^c$	$14.9^c$	Rejected as noise
—	271.2463	−27.0928	$7563.0933^c$	$0.270^c$	$12.8^c$	Rejected as flare
—	271.3306	−27.2857	$7535.4776^c$	$1.369^c$	$26.6^c$	Rejected as variable

Note. <sup>a</sup>Barycentric Julian date – 2450 000. Values for rejected lenses are at maximum flux. <sup>b</sup>Analysed in full in companion paper (Specht et al., in preparation), as a star–planet binary lens with ground-based detection. <sup>c</sup>Approximate values based on automatic modelling, assuming  $u_0 = 1$ .

(Table 4) shows a steep rise and slow decline, reminiscent of a stellar outburst. The ‘noise’ case showed periodic variability, neither clearly astrophysical nor instrumental in nature. This leaves eight candidate novel microlensing events.

#### 9.4 Object re-extraction and centring

The eight new candidates were then re-extracted using MCPM in a finer grid (21.6 arcsec  $\times$  21.6 arcsec, step size 0.72 arcsec), centred on their repositioned RA and Dec. The parameters were changed to extract only a smaller area, minimizing effects of blended stars: four pixels were selected, and a training set of 100 pixels was used, with the 10 largest outliers removed. Each light curve was also fitted with a microlensing model, using a tolerance ten times more strict than previously.

Using this grid, objects were re-centred as previously. Events at  $(\alpha, \delta) = (268.6613, -28.6140)$  and  $(268.8945, -28.4774)$  were not re-centred, as multiple sources of variability contribute to their light curves. Table 5 lists the final positions, which we expect to be accurate to  $\lesssim 2$  arcsec.

#### 9.5 Detailed inspection

Each candidate was checked against the Simbad<sup>15</sup> and VizieR<sup>16</sup> data bases. Objects within one *Kepler* pixel were identified as potential counterparts, and objects  $\lesssim 0.004$  away were considered contaminants. A summary of each is given below: three candidates are rejected and five remain.

##### 9.5.1 Rejected events

A —  $\alpha = 270^\circ 9172$ ,  $\delta = -27^\circ 2671$ . The second recentering decreased significance and increased correlated noise related to spacecraft motion. Two nearby areas of strongly negative differential flux nearby could indicate hot pixels or flat-fielding errors. The event is close (0.4 arcsec) to the 19th magnitude star *Gaia* DR2 4063147780540495872, and lies in a very dense stellar field. As there is no clear event and clear correlated noise, we dismiss this candidate as instrumental noise.

B —  $\alpha = 271^\circ 2463$ ,  $\delta = -27^\circ 0928$ . This is close (0.5 arcsec) to a 19th magnitude star in the Panoramic Survey Telescope and

Rapid Response System Data Release 1 (Flewelling et al. 2020), Pan-STARRS DR1 75482712462919121. The re-centred light curve shows a cleanly extracted, symmetrical peak. However, the flux before and after the peak shows distinct asymmetry, so we reject this candidate as a stellar flare.

C —  $\alpha = 271^\circ 3306$ ,  $\delta = -27^\circ 2857$ . This event is contaminated by a surrounding group of highly blended,  $\sim 16$ th magnitude stars. The re-centred light curve shows a faint signal with a period of  $\sim 5.6$  d, and it is likely that this unknown variable contributes a variable portion of the pixel’s flux, as the other stars in the asterism move in and out of the pixel and contribute differently through the intra-pixel response. Consequently, we dismiss this candidate as a variable star.

##### 9.5.2 Accepted events

The final five events are assigned simples (K2C9-2016-BLG-1 through -5), and their light curves shown in Fig. 9. These represent data extracted by MCPM on the re-centred candidate position, assuming a flat-prior light curve. Fitting of these events is performed in Section 11.1.2.

1 – This event is very well isolated from contaminating variables and other stars, and cleanly extracted at  $\alpha = 267^\circ 9363$ ,  $\delta = -28^\circ 9216$ . Only two objects exist within 4 arcsec: Pan-STARRS DR1 73292679366134218 (1.0 arcsec away) 73292679356504208 (1.9 arcsec away).

2 – This event is well isolated but is centred near a pixel boundary. Consequently, the event is subject to substantial intra-pixel variation, so does not appear entirely symmetrical. Two DECaPS sources are recorded within 4 arcsec.

3 – This faint, but clean event has two components: one broad and one narrow. The narrow peak occurs a few hours after the broader one. One explanation is a caustic crossing of a binary lens, but this may still be an unusual stellar flare. The eclipsing binary OGLE BLG-ECL-224994 ( $P = 1.28$  d) is 8 arcsec away: this slightly contaminates the PSF, but does not significantly affect the light curve. Mild light-curve structure is seen in the days following the event, however we accept this candidate on the balance of evidence.

4 – This source is close (0.5 arcsec) to the 18th magnitude star *Gaia* DR2 4062799265608424320, and is 8.9 arcsec south of the bright ( $B = 13.82$  mag) early-type star OPS 1759204-273316 (Grosbøl 2016). Noise from the latter causes the strongly positive and negative flux in Fig. 10. The small-amplitude red giant OGLE BLG-LPV-160527 is 18 arcsec away (Soszyński et al. 2013), but does not affect the light curve.

<sup>15</sup><http://simbad.u-strasbg.fr/>

<sup>16</sup><https://vizier.u-strasbg.fr/>

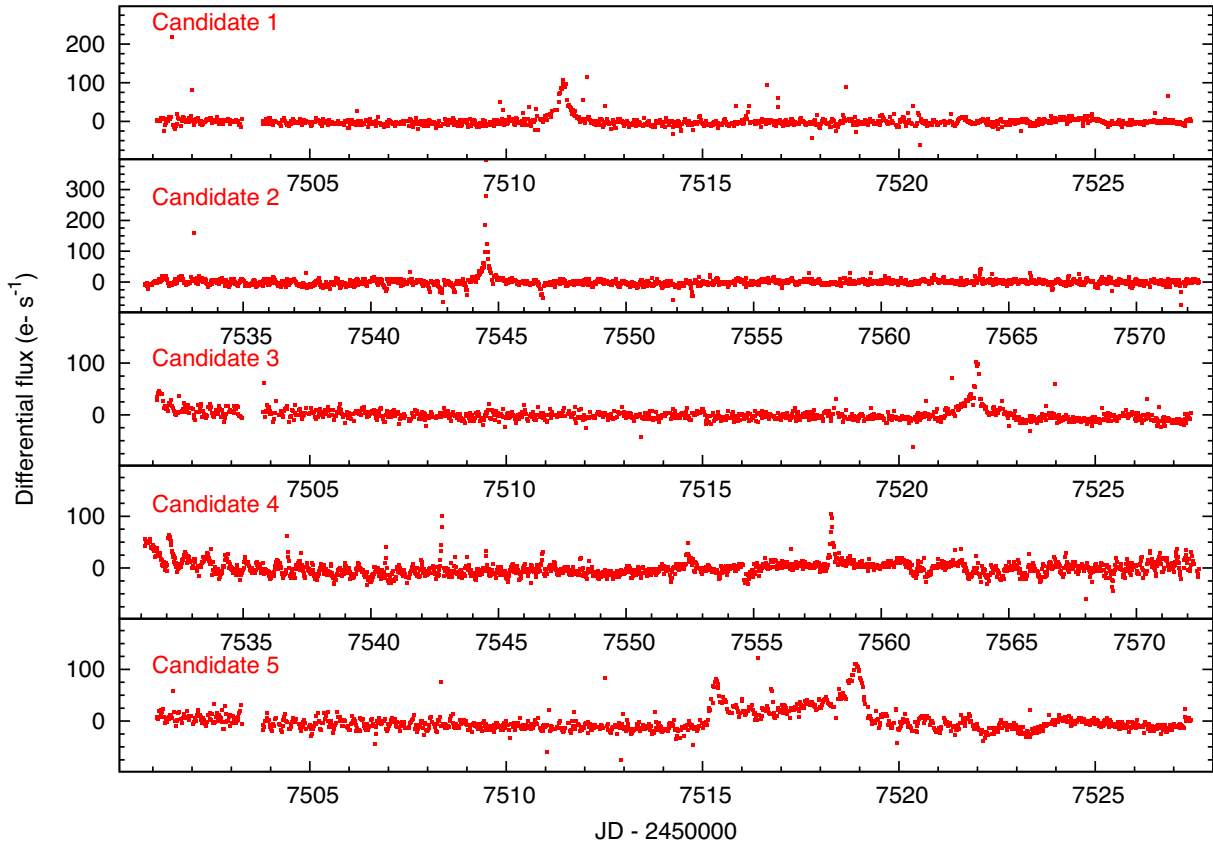


**Figure 9.** Light curves of new candidate microlensing events, extracted using MCPM by assuming a flat baseline flux model throughout, with identifiers from in Table 5. The data points are described in Section 9.

5 – This event is strong and cleanly extracted at  $\alpha = 269.^{\circ}8799$ ,  $\delta = -27.^{\circ}6079$ . The light curve showed two peaks, typical of a binary microlensing event. The eclipsing binary OGLE BLG-ECL-232395 exists at 16 arcsec from the target (Soszyński et al. 2016), but does not affect the light curve.

## 10 COMPARISON WITH EXTERNAL DATA SETS

Despite our careful vetting, external comparison is needed to verify our candidates as microlensing events.

### 10.1 OGLE

Event 1 falls between a gap in the OGLE detectors, so was not recorded. Events 2, 3, and 4 were not clearly recorded due to gaps in the OGLE coverage caused by poor weather conditions. These gaps span the following periods:

- 2 – HJD 2457536.79 to 7545.59 (*K2* event at 7544.48);
- 3 – HJD 2457519.88 to 7522.65 (*K2* event at 7522.65);
- 4 – HJD 2457557.91 to 7561.51 (*K2* event at 7558.20).

Manual inspection of individual OGLE objects around these spatial locations could not find OGLE counterparts to our events. This suggests either: (a) that these events are not real or at much lower magnification at Earth; (b) that these events were sufficiently short-time-scale not to show up in the OGLE data, despite OGLE observations often only narrowly missed the *K2* event peak; or (c)

that these events were offset in time (by microlens parallax) so that they fall entirely within the gaps in the OGLE data. The example of KMT-2016-BLG-2554 shows that more than one of these reasons could be simultaneously true. Event 5 was recovered by OGLE at position  $\alpha = 269.87983$ ,  $\delta = -27.60747$  and shows multiple peaks between HJD 2457512 and 7517.

### 10.2 KMTNet

KMTNet data for these positions are not publicly available. Examination of nearby events suggests that all five candidates should have data within 24 h of the *K2* peak, so should have been detected if they are true events that received similar magnification in the Earth’s line of sight.

### 10.3 Canada–France–Hawaii Telescope (CFHT)

CFHT observed the *K2C9* superstamp with the MegaCam wide-field imager several times per night in the *g*-, *r*-, and *i*-bands, aiming to measuring the colours of any short-time-scale FFP candidates. MegaCam was only mounted on the telescope for four 2-week runs at or around the time of the *K2C9*. Full details of the observations and their reduction are provided by Zang et al. (2018). Difference images produced using ISIS (Alard & Lupton 1998; Alard 2000) were visually inspected within  $\sim 6$  arcsec of the candidate locations for the duration of the observations.

Candidate 1 returns a strong visual source at  $(\alpha, \delta)_{ICRS} = (267.93612, -28.92149)$  in two *i*-band difference images taken at

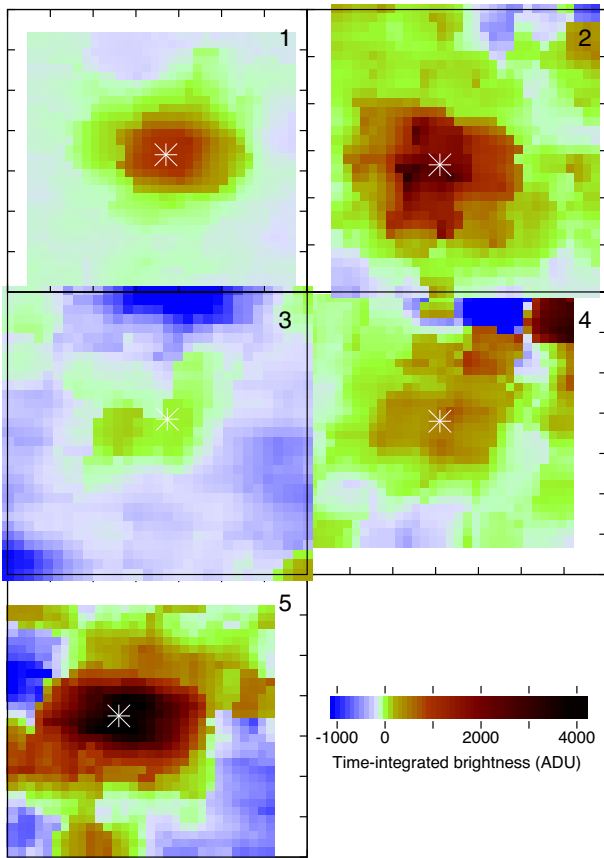


**Figure 10.** Relative integrated brightness of events over a sub-pixel-sampled region. Each box is  $0.^\circ006 \times 0.^\circ006$ . Brightness increases towards darker, redder colours, and is defined as the integrated flux of the extracted (differential) light curve within the time range  $t_0 \pm \tau_0/2$ . Negative brightness show decreased flux compared to the baseline. White asterisks mark the adopted location of each source.

$\text{BJD}' = 7511.02$  and  $7511.98$ , but not in the next two nearest images at  $\text{BJD}' = 7510.12$  and  $7513.04$ . The source was not visible in  $r$ - or  $g$ -band images taken nearly coincidentally, but the region is heavily reddened [ $A_i = 3.93 \pm 0.04$ ,  $E(r-i) = 1.54 \pm 0.02$ ], estimated based on the location of the red clump using the same method as (Nataf et al. 2013) and assuming the intrinsic colour of the clump from (Nataf et al. 2016). Photometry at the location in the  $r$ -band reveal a marginal detection of flux in a single image at  $\text{BJD}' = 7511.98$ .

Candidate 2 was observed in two overlapping CFHT fields, CF1 and CF6. Observations were obtained at least daily during the third MegaCam run ( $\text{BJD}' = 7538.1$  and  $7548.0$ ) with only one gap, between  $\text{BJD}' = 7545.07$  and  $7546.94$ . No source was visually identified in CF6, but in CF1 a marginal visual detection was identified at  $(\alpha, \delta)_{\text{ICRS}} \approx (268.66129, -28.61404)$  in an  $i$ -band image at  $\text{BJD}' = 7542.91$ . The nearest CF6 image was taken 6 min later, so we expect that the visual detection in CF1 was spurious. A possibility remains that a short event occurred in the one-night observing gap.

Candidate 3 was not visually detected, but the  $K2$  event was at the end of a MegaCam run. If the ground-based event peaked after the  $K2$  event, we would not expect a detection.

Candidate 4's event occurred between MegaCam runs and was likewise not visually detected.

Candidate 5 was visually detected in several images in  $g$ -,  $r$ -, and  $i$ -bands at  $(\alpha, \delta)_{\text{ICRS}} = (269.87984, -27.60736)$  between  $\text{BJD}'$

$\sim 7511$  and  $7516$ . The light curve shows two sharp peaks upon a shallow decline throughout the observations, indicative of a planetary or secondary caustic crossing in the wing of a microlensing event with a reasonably long time-scale.

## 11 DISCUSSION

### 11.1 Candidate properties

#### 11.1.1 Summary of status

Our analysis has revealed five new candidate microlensing events in the  $K2C9$  data. Candidates 3 and 4 have no ground-based observations. Comparative ground-based light curves for candidates 1, 2, and 5 are shown in Fig. 11, and in more detail in the online Appendix. For candidates 1 and 5, we update the astrometry (Table 5) based on the average of the OGLE and CFHT positions.

Visual inspection of the CFHT images suggests candidate 1 may be associated with Pan-STARRS DR1 73292679366134218, which is recorded at  $i = 22.173 \pm 0.077$ ,  $z = 20.820 \pm 0.099$ ,  $y = 20.493 \pm 0.223$  mag in that survey. The strong drop-off with increasing wavelength is consistent with a cool or highly extinguished star, explaining the significant differences in differential flux between the CFHT  $r$ - and  $i$ -band light curves. Ground-based data show a peak that is roughly co-incident with the  $K2C9$  peak, showing this is an astrophysical event, consistent with a microlensing source. However, without a clear time or magnitude offset, we cannot rule out other kinds of event (e.g. stellar flares). Hence, this object remains a candidate event only.

Candidates 2, 3, and 4 show the hallmarks of real events but, without ground-based confirmation, we cannot correctly assign them to any particular category. Given the availability of terrestrial observations, we treat candidate 2 as a potential microlensing event with no perceptible magnification on Earth, but stop short of claiming it as a real event. We treat candidates 3 and 4 as suspected events, but without the ability to confirm or refute them. In particular, we note that candidates 3 and 4 have noticeable asymmetries in their light curves: these are small, and ultimately could be attributable to the structured noise terms seen in real events (see online Appendix, e.g. OGLE-2016-BLG-014 and -1231, and KMT-2016-BLG-0162).

#### 11.1.2 Fitting of candidate parameters

In Poleski et al. (2019), the analysed events had ground-based data that constrained  $t_E$ , which is usually the same to within a few per cent for ground and satellite observations of a given event.<sup>17</sup> Our four new single-lens candidate events have very sparse ground-based data that do not allow the event time-scale to be meaningfully constrained. To measure the microlensing parallax using the time-scale measured in the  $K2$  data, one needs to constrain  $t_{0,\oplus}$  and  $u_{0,\oplus}$  plus the source and blending fluxes from ground-based data. However, the existing data are too sparse to constrain these parameters. The sparsity of the ground-based data is easily understood: if these events had more epochs from microlensing surveys, it is likely that the surveys would have discovered them in the first place. Hence, we decided to only fit the  $K2$  data without constraining the microlensing parallax.

<sup>17</sup>The difference in time-scale of the event for different observers will depend on their relative velocity tangential to the line of sight to the event ( $\lesssim 30$  km  $\text{s}^{-1}$ ) and the projected velocity of the lens-source line of sight across the Solar system ( $\sim 100$ – $1000$  km  $\text{s}^{-1}$ , e.g. Calchi Novati et al. 2015).

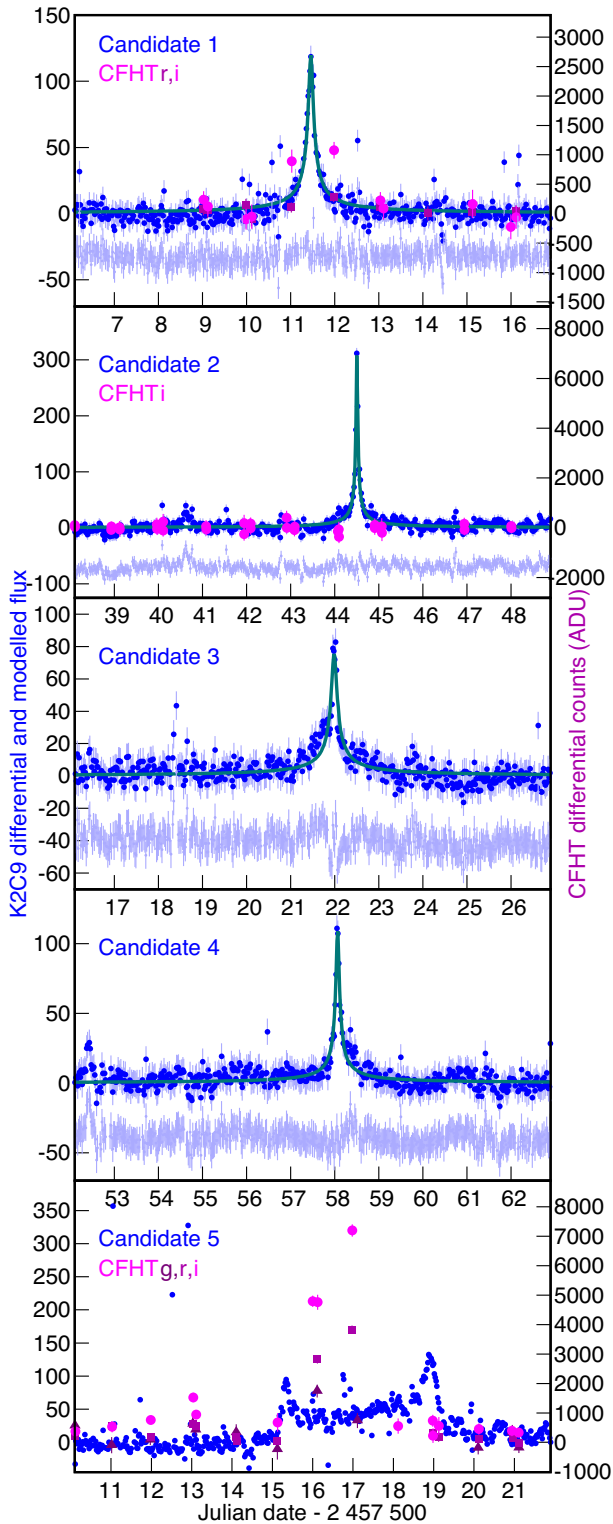


**Figure 11.** K2C9 light curves of new FFP candidates with ground-based observations. K2 observations are shown as blue points, with the corresponding model as a cyan line. Residuals are shown in light blue, offset below. Candidate 5 is modelled separately in Specht et al. (in preparation). Observations from CFHT are shown in purple, approximately scaled to the same intrinsic flux.

MCPM has not previously been used for events without ground-based data. To test the method, we fitted a four-parameter Paczyński model (with zero baseline flux 0) to the K2 data for events analysed by Poleski et al. (2019). These fits revealed that the model is too flexible and it overfits the noisy data, resulting in significantly underestimated  $t_E$ . The other possible approach is to use a pixel-lensing model, in which the excess flux is fitted by a three-parameter model:  $t_0$ ,  $\Delta F \equiv F_s/u_0$  (where  $\Delta F$  is the change in flux and  $F_s$  is the source flux), and  $t_{\text{eff}}$  (Gould 1996). The smaller the value of  $u_0$ , the better the pixel-lensing approach approximates Paczyński equation. Other than this simplified model, the fitting followed Poleski et al. (2019), i.e. the light curve was simultaneously extracted and fitted, the photometry was extracted for four central pixels, 500 training pixels were used in the first step, then limited to 100 pixels, and L2-regularization factor was set to 6000 per pixel. As a consistency check, we fitted events analysed by Poleski et al. (2019) and found that the formal uncertainties on the fitted  $\Delta F$  and  $t_{\text{eff}}$  are underestimated, but that these parameters are accurate to  $\approx 10$  per cent. The results of the parameter inference for the four new candidate events are presented in Table 5 and shown in Fig. 11. The fits for the previously known OGLE/KMTNet events that were selected by our pipeline are presented in the online Appendix. We note that for candidates 1 and 2, the peaks of the final light curves are brighter than those extracted in Section 2.2.

### 11.2 A new bound microlensing event

Candidate 5 is clearly recovered in terrestrial data, but with a light curve with peaks that do not match the timing from K2. These differences show that the event is not intrinsic to the source, but caused by a previously unknown microlensing event. The shape of the event in K2 and ground-based data is consistent with a binary lens, with the primary-lens peak visible in only the ground-based data, near HJD 2457513. Caustic crossings then occur in the ground-based data at dates  $\approx 7515.6$  and  $7516.9$ , and in the K2 data at dates 7515.3 and 7518.9. Visual inspection of the CFHT images shows the event to be associated with a faint but resolved star, currently without a designation. It is unresolved from two close neighbours and two nearby brighter stars (Pan-STARRS DR1 74872698800561822 and 74872698803761694) in the PanSTARRS and DECaPS surveys. Modelling of this lens is presented in a companion paper (Specht et al., in preparation).

### 11.3 Free-floating planets versus stellar-mass lenses

Although FFP microlensing events separate well from stellar-mass events in  $t_E$ , the same has not been demonstrated for  $t_{\text{eff}}$ . To show this, we have simulated a population of microlensing events using the MaB $\mu$ LS-2 simulator (Specht et al. 2020) optimized to K2 parameters. By computing both the  $t_E$  and  $t_{\text{eff}}$  for each simulated microlens, we can compute the stellar and brown dwarf  $t_{\text{eff}}$  distribution shown in black in Fig. 12.

For FFP calculations we replace each lensing star with a planetary-mass lens that inherits its position and kinematics, thus generating the expected  $t_{\text{eff}}$  distribution for Jupiter and Earth mass FFP populations. Scaling these to 1.8 Jupiter-mass FFPs per star (as discussed in Sumi et al. 2011), and 10 Earth-mass FFPs per star (as discussed in Mróz et al. 2017), and adding them to the stellar-mass distribution, we generate the combined FFP–stellar  $t_{\text{eff}}$  distributions shown as coloured lines in Fig. 12.

These distributions assume an event recovery that is independent of  $t_{\text{eff}}$ . In reality, the recovery efficiency depends on the relative

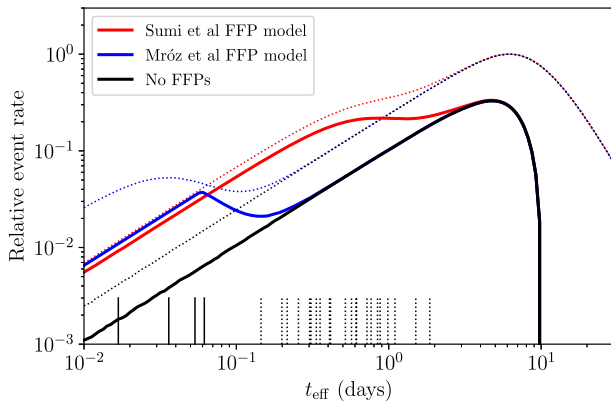


**Figure 12.** The predicted  $t_{\text{eff}}$  distribution for microlensing events towards the K2C9 field for stars and brown dwarfs (black), with the addition of either the Jupiter (Sumi et al. 2011, in red) or Earth (Mróz et al. 2017, in blue) FFP models. Thin, dotted lines show the full distributions, in the limit of uniform detection efficiency. Thick, solid lines show the distributions when events are windowed to  $0.06 \text{ d} < t_E < 10 \text{ d}$ . Vertical lines at the plot's base show our four candidate FFP events (solid lines), and our  $t_{\text{eff}}$  fits to K2C9 data of the OGLE/KMTNet events presented in the online Appendix (dashed lines).

sensitivity of the underlying photometry, and the selection effects of our pipeline's smoothing functions. The efficiency function cannot be described without complex simulations (Specht et al., in preparation), but we expect roughly equal sensitivity over the range  $0.083 \text{ d} \lesssim t_{\text{eff}} \lesssim 2 \text{ d}$ , with a smooth decline in sensitivity at both ends. The solid lines in Fig. 12 show the effect of a more conservative windowing function of  $0.06 \text{ d} < t_{\text{eff}} < 10 \text{ d}$  that is applied in our pipeline.

Fig. 12 also indicates the  $t_{\text{eff}}$  of our four new candidate FFP events, and the previously known events from OGLE and KMTNet that pass our selection pipeline. The known events scatter around  $t_{\text{eff}} \approx 0.6 \text{ d}$ , and are in line with the short- $t_{\text{eff}}$  tail of a stellar distribution. The lack of sources with  $t_{\text{eff}} \gtrsim 1 \text{ d}$  implies declining sensitivity beyond this point. The  $t_{\text{eff}}$  of our four candidate FFP sources is an order of magnitude or more shorter than this peak. While firm conclusions can only be drawn after we complete our efficiency analysis (Specht et al., in preparation) their time-scales are consistent with the peak expected for the Earth-mass FFP model. As such they are perhaps the most promising FFP candidates recovered from K2.

#### 11.4 Frequency of free-floating planets

A thorough evaluation of the FFPs frequency is in progress (Specht et al., in preparation) and requires a Galactic model description of the FFP distribution and a determination of the event recovery efficiency through our K2C9 selection pipeline. Nevertheless, we can here make some quantitative statements on the FFP abundance and the probability that our candidates represent a genuine FFP population.

Penny et al. (2017) calculated the potential K2C9 FFP yield, estimating that 1.1–6.3 events would be detectable [based on the higher Sumi et al. (2011) FFP abundance, and including the 20 per cent loss due to K2 entering emergency mode]. The majority (roughly 60–85 per cent) of these would be simultaneously detectable by ground-based observatories, with most of the remainder having an Einstein ring that crosses *Kepler's* orbit but not Earth's. Crucially, short-time-scale FFPs separate well from stellar lenses in terms of their Einstein radii (e.g. Penny et al. 2017, their fig. 3), with FFPs peaking around the separation of K2 from Earth, and stars having much larger Einstein radii. This means that single-lens events (where caustic crossings do not exist) present large differences in amplitude

between K2 and Earth if the lens is an FFP, but not if the lens is a star. Candidate FFPs therefore include

- (i) K2 events not recovered by terrestrial observatories;
- (ii) terrestrial events that are not recovered by K2;
- (iii) events detected at both sites with large time and/or magnification differences.

The first category includes our events K2C9-2016-BLG-2, -3, and -4, which appear to have been undetectable from Earth. If these are indeed astrophysical events, their lack of terrestrial detection adds weight to their being true microlensing events with projected Einstein radii  $\lesssim 1 \text{ au}$ . However, without ground-based confirmation, we cannot determine their nature with confidence. Consequently, we can say that there are 0–3 detected events in this category.

The second category contains some of the events in Section 3.1 that were not visible in the K2 light curves: five OGLE events (OGLE-2016-BLG-1041, -1058, -1110, -1097, and -1162) and 10–18 KMTNet events, depending on whether the events weakly visible by eye are included. Generally, these events are confirmed as astrophysical via observation by more than one terrestrial observatory. However, the heavy blending and sensitivity differences (notably due to the bluer  $K_p$  filter and heavy interstellar reddening of the source stars) mean we cannot expect all of these would be detectable by K2, but this would require extensive modelling to determine the dilution by blending. There are also significant uncertainties on the  $t_E$  and/or  $t_{\text{eff}}$  of some events, particularly in the KMTNet data set, hence we cannot confidently determine the simple of short-time-scale microlensing events either.

The third category does not include any of our novel FFP events, but does include K2C9-2016-BLG-5 that is due to a bound planet. Some of the four events discussed in Section 8.4 may also fall into this category.

Whilst we cannot yet unambiguously confirm FFPs from the K2C9 dataset, we have identified several short-time-scale events that are promising candidates. We know from events such as OGLE-2016-BLG-1928 (Mróz et al. 2020), which lies just outside the K2C9 field of coverage, and OGLE-2016-BLG-1540 (Mróz et al. 2018), which occurred inside the field of coverage but after the cessation of observations, that FFPs can be expected. Hence, at this point, it is certainly credible that the simples of recovered FFPs are in line with Penny et al. (2017) estimates. Comparison against other (proprietary) sources of ground-based data may confirm some of our novel candidates, and improved modelling of our recovery of known ground-based candidates may confirm some of these short-time-scale events as FFPs.

#### 11.5 Lessons for future microlensing space missions

##### 11.5.1 Event detection and isolation

K2C9 (and previous *Spitzer* surveys, e.g. Calchi Novati et al. 2015; Yee et al. 2015) act as a pathfinders for dedicated microlensing surveys using upcoming space-based facilities: a significant effort has already been expended formulating microlensing surveys for *Euclid* (Laurijs et al. 2011) and the *Nancy Grace Roman Space Telescope* (formerly *WFIRST* and hereafter referred to as *Roman*; Green et al. 2012; Penny et al. 2019; Johnson et al. 2020). This work demonstrates that blind space-based microlensing surveys are possible. Indeed the considerable challenges posed by the sub-optimal nature of the K2C9 dataset for microlensing analyses provide an extreme stress-test that allows us to push forward into the space-based microlensing era with confidence.

The most significant issues affecting *K2C9* were ultimately due to (in order of precedence): the telescope's large (4 arcsec) pixel size compared to the high sky density of stars towards the Galactic bulge, the undersampling of the PSF with respect to this pixel size, and the spacecraft motion caused by the lack of gyroscopic control in the extended *K2* mission.

*Pixel scale:* *Kepler's* large pixel scale means each pixel represents the overlapping PSFs of many stars and asteroids: the Dark Energy Camera Plane Survey (DECaPS; Schlafly et al. 2018), the deepest large-scale survey of the region, averages  $\sim 7$  stars per *Kepler* pixel, not including stars missing due to its own blending incompleteness, and the many microlensing sources below the detection threshold. This makes event localization very difficult, but also means that issues affecting a small percentage of stars can make large areas of the detector unusable. In *K2C9*, this included variable stars, many of which have not been adequately catalogued, especially low-amplitude or sporadic variables. Saturated stars and asteroids also mean large regions of the detector are masked, but these can be more easily identified and accounted for. Pixel artefacts also posed significant problems, including those with large dark currents and/or are poorly flat-fielded.

Both *Euclid's* visible instrument and *Roman's* near-infrared camera will observe several magnitudes deeper than *K2C9*. However, their pixels (0.1 and 0.11, respectively) have areas  $\sim 1500\times$  smaller, more than compensating for the increased source density. Simulated images, using population-model data (Penny et al. 2013, 2019), suggest that individual stars will be much more cleanly resolved than with *K2* (cf. Penny et al. 2017), and that microlensing sources will be much more cleanly identified. Hence, we expect these to be much less severe for *Euclid* and *Roman*.

*PSF undersampling and aberration:* *Kepler* suffered from significant PSF undersampling: 20–62 per cent of a star's flux fell in a single pixel,<sup>18</sup> and the strong intra-pixel response function varied by a factor of 2 across a pixel (Bryson et al. 2010). Without knowing an event's precise intra-pixel co-ordinates, these led to the significant variations in the flux received from both the source star and its blended neighbours, producing the strong correlated-noise signals of our data. This occurs despite the telescope PSF and camera intra-pixel response function being well-characterized. It also exacerbates small errors in dark subtraction and flat-fielding: these alone often dominate over the photonic Poisson noise.

Additionally, *Kepler* exhibited strong aberration. The *K2C9* superstamp was at the edge of the field of view, due to ecliptic-plane restrictions. This led to a bright PSF core, causing the problems just highlighted, while spreading a small fraction of the star's flux out over many pixels, exacerbating the aforementioned problems of stellar crowding.

*Euclid* VIS and *Roman* both have 50 per cent encircled energy radii of  $\sim 0.13$  arcsec (i.e. half the star's flux is contained within this radius, or within central  $\sim 4$ –6 pixels).<sup>19</sup> Consequently, the PSF undersampling is still significant, but a factor of several less than *Kepler*. The intra-pixel quantum efficiencies for *Euclid* VIS and *Roman* have yet to be formally released. Their smaller overall field of view and on-axis pointing will also reduce the effects of PSF aberration.

*Spacecraft motion:* broken reaction wheels meant *K2* lacked good gyroscopic control. *Euclid* and *Roman* will not have such problems.

Diffraction spikes from bright stars, caused by the secondary mirror supports (three for *Euclid*, six for *Roman*) may rotate around the frame, causing spurious brightenings. However, most of the problem sources in *K2C9* were caused by blended stars, not the motion on the detector of the source star images themselves, so we correlated noise to be a present but lesser problem for the future missions.

### 11.5.2 False-positive rejection

In the *K2C9* data, false positives were removed in approximate order of ease of separation from true microlensing signals. Most artefacts related to spacecraft motion can be removed through correlation of the light curve with the spacecraft pointing vector (though the correlation will be different for every star). We have shown that these motions can be accounted for relatively easily and, with a better-sampled PSF and better resolution, such false positives should be much easier to characterize. Similarly, with a wider PSF, a sharpness criterion could be used to differentiate cosmic ray impacts from stellar brightening events.

Variable stars and asteroids are significant false positives in our data. Recognition and removal of asteroids was fairly straightforward, but the variable star catalogues we used are incomplete. We can expect their completeness to improve through ongoing surveys like OGLE, and new surveys like the Vera Rubin Observatory (formerly LSST; Ivezić et al. 2019).

One of the last false-positive categories we removed was stellar flares. In the era of *Euclid* and *Roman*, these may prove the most tenacious category of false positive. With better resolution and PSF sampling comes lower instrumental noise, and it should be easier to determine whether light curves are genuinely skewed, rather than merely appearing so due to the varying PRF. However, the fundamental limit to detecting skewness is the simple of exposures that happen during the event. Many of the stellar flares in this data set are not strictly sudden onset, but occur after unresolved 'foreshocks', and still lead to a markedly skewed light curve, but not an instantaneous brightening. In general, our 30-minute cadence produced a limit whereby events shorter than  $\sim 2$ –4 h could not readily be differentiated from stellar flares. However, we must bear in mind that this is partly due to the need for adaptive photometric methods like MCPM due to the large pixel scale. Analysis of *Euclid* and *Roman* data will make use of highly precise difference image photometry pipelines, allowing very high-precision cuts to be implemented on overall light-curve smoothness and symmetry that will provide greater screening against stellar flare event.

### 11.5.3 Event confirmation

Despite the limitations of the *K2* mission, we have shown the viability of space-based microlensing surveys. We have also demonstrated their potential to identify and characterize parallax effects when combined with ground-based observations, leading to the confirmation of exoplanetary candidates.

This added dimensionality, coming from taking multiple chords through the Einstein ring of the microlens, is only possible with a good quality of ground-based observation. The new events described here were primarily missed from ground-based observatories because they did not coincide with either the hours of darkness or clear weather. Consequently, if future space-based microlensing surveys have complementary observations from ground-based observatories with high ( $\lesssim$ hourly) cadence observations and redundancy for

<sup>18</sup><https://keplerscience.arc.nasa.gov/the-kepler-space-telescope.html>.

<sup>19</sup>[https://roman.gsfc.nasa.gov/science/sdt-public/WFIRST-AFTA\\_SDT\\_Report\\_150310\\_Final.pdf](https://roman.gsfc.nasa.gov/science/sdt-public/WFIRST-AFTA_SDT_Report_150310_Final.pdf).

weather and technical limitations, the events that are bright enough to be detected from the ground will be characterized better.

## 12 CONCLUSIONS

We have performed a blind search for new candidate microlensing events in the K2 Campaign 9 observations of a  $3.7 \text{ deg}^2$  region of the Galactic bulge, focussing on detection of systems with Einstein-crossing time-scales between approximately 2 h and 2 d. Considering all time-scales, we recovered 22 known events and detected four FFP candidates, and one new, bound planet. One of our candidates was recovered in the ground-based data, confirming it as astrophysical, but for none of these events has  $t_E$  been measured reliably. Thus, the simple of FFP candidates from K2C9 is between zero and four. This simple was predicted by Penny et al. (2017) to be 1.1–6.3 based on the Sumi et al. (2011) FFP rate. The FFP rate was measured by Mróz et al. (2017) using a larger sample of events and found an upper limit seven times smaller than the Sumi et al. (2011) result, which accordingly scales the Penny et al. (2017) prediction.

In this analysis, a bespoke reduction process was necessary due to the poor resolution and complex systematics of K2. Looking ahead to upcoming space missions (*Euclid* and *Roman*), we are optimistic they can recover short-time-scale microlensing events, as the systematic issues that affected K2 should be less significant. Our most significant concern with these new missions is their ability to accurately separate short-time-scale events from stellar flares and have sufficient ground-based follow-up so that short-time-scale events can be reproduced despite daylight and weather restrictions.

## ACKNOWLEDGEMENTS

EK acknowledges funding by the UK Science and Technology Facilities Council (grant ST/P000649/1). This paper includes data collected by the K2 mission. Funding for the K2 mission is provided by the NASA Science Mission directorate. Some of the data presented in this paper were obtained from the Mikulski Archive for Space Telescopes (MAST). We thank OGLE team for sharing results of their observations. Work by RP was supported by Polish National Agency for Academic Exchange grant ‘Polish Returns 2019.’ This research uses data obtained through the Telescope Access Program (TAP), which has been funded by the National Astronomical Observatories of China, the Chinese Academy of Sciences (the Strategic Priority Research Program ‘The Emergence of Cosmological Structures’ Grant No. XDB09000000), and the Special Fund for Astronomy from the Ministry of Finance. This work was performed in part under contract with the California Institute of Technology (Caltech)/Jet Propulsion Laboratory (JPL) funded by NASA through the Sagan Fellowship Program executed by the NASA Exoplanet Science Institute. Work by MTP was partially supported by NASA grants NNX16AC62G and NNG16PJ32C, and Louisiana Board of Regents Support Fund (RCS Award Contract Simple: LEQSF(2020-23)-RD-A-10). This study is based in part on observations obtained with MegaPrime/MegaCam, a joint project of CFHT and CEA/DAPNIA, at the Canada–France–Hawaii Telescope (CFHT) which is operated by the National Research Council (NRC) of Canada, the Institut National des Sciences de l’Univers of the Centre National de la Recherche Scientifique (CNRS) of France, and the University of Hawaii. The authors wish to recognize and acknowledge the very significant cultural role and reverence that the summit of Mauna Kea has always had within the indigenous Hawaiian community. We are most fortunate to have the opportunity to conduct observations from this mountain. SM and WZ acknowledge support by the National Science

Foundation of China (Grant No. 11821303 and 11761131004). WZ was supported by the Natural Sciences and Engineering Research Council of Canada (NSERC) under the funding reference #CITA 490888-16. We finally thank the anonymous referee for constructive feedback.

## DATA AVAILABILITY

The underlying data for this work is in the public domain, and sourced from the Mikulski Archive for Space Telescopes, <https://archive.stsci.edu/k2/>. Third-party data from OGLE and the CFHT were provided by co-authors RP and MP, respectively, and will be shared on reasonable request to the corresponding author, subject to the permission of the relevant observing groups. The analysis tools developed for this article are considered bespoke, but can be shared on reasonable request to the corresponding author.

## REFERENCES

- Alard C., 2000, *A&AS*, 144, 363  
 Alard C., Lupton R. H., 1998, *ApJ*, 503, 325  
 Ban M., Kerins E., Robin A. C., 2016, *A&A*, 595, A53  
 Bihain G. et al., 2009, *A&A*, 506, 1169  
 Borucki W. J. et al., 2010, *Science*, 327, 977  
 Bryson S. T. et al., 2010, *ApJ*, 713, L97  
 Calchi Novati S. et al., 2015, *ApJ*, 804, 20  
 Clanton C., Gaudi B. S., 2017, *ApJ*, 834, 46  
 Di Stefano R., 2012, *ApJS*, 201, 20  
 Einstein A., 1936, *Science*, 84, 506  
 Flewelling H. A. et al., 2020, *ApJS*, 251, 7  
 Gahm G. F., Grenman T., Fredriksson S., Kristen H., 2007, *AJ*, 133, 1795  
 Gaia Collaboration, 2018, *A&A*, 616, A1  
 Gould A., 1996, *ApJ*, 470, 201  
 Gould A., Horne K., 2013, *ApJ*, 779, L28  
 Green J. et al., 2012, preprint ([arXiv:1208.4012](https://arxiv.org/abs/1208.4012))  
 Grosbøl P., 2016, *A&A*, 585, A141  
 Halbwachs J. L., Arenou F., Mayor M., Udry S., Queloz D., 2000, *A&A*, 355, 581  
 Han C., 2006, *ApJ*, 644, 1232  
 Han C., Chung S.-J., Kim D., Park B.-G., Ryu Y.-H., Kang S., Lee D. W., 2004, *ApJ*, 604, 372  
 Helstrom C. W., Wilson F. L., 1970, *Phys. Today*, 23, 73  
 Henderson C. B., Shvartzvald Y., 2016, *AJ*, 152, 96  
 Henderson C. B. et al., 2016, *PASP*, 128, 124401  
 Howell S. B. et al., 2014, *PASP*, 126, 398  
 Ivezić Ž. et al., 2019, *ApJ*, 873, 111  
 Johnson S. A., Penny M., Gaudi B. S., Kerins E., Rattenbury N. J., Robin A. C., Calchi Novati S., Henderson C. B., 2020, *AJ*, 160, 123  
 Kim S.-L. et al., 2016, *J. Korean Astron. Soc.*, 49, 37  
 Kim D. J. et al., 2018a, *AJ*, 155, 76  
 Kim H. W. et al., 2018b, *AJ*, 155, 186  
 Laureijs R. et al., 2011, preprint ([arXiv:1110.3193](https://arxiv.org/abs/1110.3193))  
 Libralato M., Bedin L. R., Nardiello D., Piotto G., 2016, *MNRAS*, 456, 1137  
 Lucas P. W., Roche P. F., 2000, *MNRAS*, 314, 858  
 Ma S., Mao S., Ida S., Zhu W., Lin D. N. C., 2016, *MNRAS*, 461, L107  
 Mróz P. et al., 2017, *Nature*, 548, 183  
 Mróz P. et al., 2018, *AJ*, 155, 121  
 Mróz P. et al., 2020, *ApJ*, 903, L11  
 Nataf D. M. et al., 2013, *ApJ*, 769, 88  
 Nataf D. M. et al., 2016, *MNRAS*, 456, 2692  
 Paczyński B., 1986, *ApJ*, 304, 1  
 Peña Ramírez K., Béjar V. J. S., Zapatero Osorio M. R., 2016, *A&A*, 586, A157  
 Penny M. T. et al., 2013, *MNRAS*, 434, 2  
 Penny M. T., Rattenbury N. J., Gaudi B. S., Kerins E., 2017, *AJ*, 153, 161

- Penny M. T., Gaudi B. S., Kerins E., Rattenbury N. J., Mao S., Robin A. C., Calchi Novati S., 2019, *ApJS*, 241, 3
- Poleski R., Yee J. C., 2019, *Astron. Comput.*, 26, 35
- Poleski R., Penny M., Gaudi B. S., Udalski A., Ranc C., Barentsen G., Gould A., 2019, *A&A*, 627, A54
- Quanz S. P., Goldman B., Henning T., Brandner W., Burrows A., Hofstetter L. W., 2010, *ApJ*, 708, 770
- Rasio F. A., Ford E. B., 1996, *Science*, 274, 954
- Schlafly E. F. et al., 2018, *ApJS*, 234, 39
- Schneider A. C., Windsor J., Cushing M. C., Kirkpatrick J. D., Wright E. L., 2016, *ApJ*, 822, L1
- Soszyński I. et al., 2013, *Acta Astron.*, 63, 21
- Soszyński I. et al., 2016, *Acta Astron.*, 66, 405
- Specht D., Kerins E., Awiphan S., Robin A. C., 2020, *MNRAS*, 498, 2196
- Sumi T. et al., 2011, *Nature*, 473, 349
- Sumi T. et al., 2013, *ApJ*, 778, 150
- Udalski A., 2003, *Acta Astron.*, 53, 291
- Udalski A., Pietrzynski G., Szymanski M., Kubiak M., Zebrun K., Soszynski I., Szweczyk O., Wyrzykowski L., 2003, *Acta Astron.*, 53, 133
- Udalski A., Szymański M. K., Szymański G., 2015a, *Acta Astron.*, 65, 1
- Udalski A. et al., 2015b, *ApJ*, 799, 237
- Veras D., Raymond S. N., 2012, *MNRAS*, 421, L117
- Vorobiev D., Ninkov Z., Caldwell D., Mochnacki S., 2018, in Lystrup M., MacEwen H. A., Fazio G. G., Batalha N., Siegler N., Tong E. C., eds, Proc. SPIE Conf. Ser. Vol. 10698, Space Telescopes and Instrumentation 2018: Optical, Infrared, and Millimeter Wave. SPIE, Bellingham, p. 106985J
- Wang D., Hogg D. W., Foreman-Mackey D., Schölkopf B., 2016, *PASP*, 128, 094503
- Whitworth A. P., Zinnecker H., 2004, *A&A*, 427, 299
- Witteborn F. C., Van Cleve J., Borucki W., Argabright V., Hascall P., 2011, in Shaklan S., ed., Proc. SPIE Conf. Ser. Vol. 8151, Techniques and Instrumentation for Detection of Exoplanets V. SPIE, Bellingham, p. 17
- Yee J. C. et al., 2015, *ApJ*, 810, 155
- Zang W. et al., 2018, *PASP*, 130, 104401
- Zhu W. et al., 2017, *PASP*, 129, 104501

## SUPPORTING INFORMATION

Supplementary data are available at [MNRAS](https://academic.oup.com/mnras/article/505/4/5584/6315707) online.

### k2c9\_appendix.pdf

Please note: Oxford University Press is not responsible for the content or functionality of any supporting materials supplied by the authors. Any queries (other than missing material) should be directed to the corresponding author for the article.

This paper has been typeset from a  $\text{\TeX}/\text{\LaTeX}$  file prepared by the author.